IVYSPRING INTERNATIONAL PUBLISHER

Theranostics

2014; 4(7): 721-735. doi: 10.7150/thno.9052

Research Paper

Luminescent Dual Sensors Reveal Extracellular pH-Gradients and Hypoxia on Chronic Wounds That Disrupt Epidermal Repair

Stephan Schreml[1]✉, Robert J. Meier[2], Michael Kirschbaum[3], Su Chii Kong[4], Sebastian Gehmert[5], Oliver Felthaus[6], Sarah Küchler[7], Justin R. Sharpe[8], Kerstin Wöltje[3], Katharina T. Weiß[1], Markus Albert[1], Uwe Seidl[1], Josef Schröder[9], Christian Morsczeck[6], Lukas Prantl[5], Claus Duschl[3], Stine F. Pedersen[4], Martin Gosau[6], Mark Berneburg[1], Otto S. Wolfbeis[2], Michael Landthaler[1], Philipp Babilas[1]

1. Department of Dermatology, University Medical Center Regensburg, Franz-Josef-Strauss-Allee 11, 93053 Regensburg, Germany
2. Institute of Analytical Chemistry, Chemo- and Biosensors, University of Regensburg, Universitätsstraße 31, 93053 Regensburg, Germany
3. Fraunhofer Institute for Biomedical Engineering, Branch Potsdam, Am Mühlenberg 13, 14476 Potsdam, Germany
4. Department of Biology, University of Copenhagen, 13 Universitetsparken, DK-2100 Copenhagen, Denmark
5. Center of Plastic Surgery, Department of Trauma Surgery, University Medical Center Regensburg, Franz-Josef-Strauss-Allee 11, 93053 Regensburg, Germany
6. Department of Maxillofacial Surgery, University Medical Center Regensburg, Franz-Josef-Strauss-Allee 11, 93053 Regensburg, Germany
7. Department of Pharmacy, Freie Universität Berlin, Königin-Luise-Str. 2-4, 14195 Berlin, Germany
8. Blond McIndoe Research Foundation, Queen Victoria Hospital, Holtye Road, East Grinstead RH19 3DZ, England, UK
9. Center for Electron Microscopy at the Institute of Pathology, University Medical Center Regensburg, Franz-Josef-Strauss-Allee 11, 93053 Regensburg, Germany

✉ Corresponding author: Stephan Schreml, M.D. Department of Dermatology, University Medical Center Regensburg, Franz-Josef-Strauss-Allee 11, 93053 Regensburg, Germany. T: +49-(0)941-944-9614; F: +49-(0)941-944-9611; M: stephan@schreml.de

Received: 2014.03.09; Accepted: 2014.04.04; Published: 2014.04.30

Abstract

Wound repair is a quiescent mechanism to restore barriers in multicellular organisms upon injury. In chronic wounds, however, this program prematurely stalls. It is known that patterns of extracellular signals within the wound fluid are crucial to healing. Extracellular pH (pH_e) is precisely regulated and potentially important in signaling within wounds due to its diverse cellular effects. Additionally, sufficient oxygenation is a prerequisite for cell proliferation and protein synthesis during tissue repair. It was, however, impossible to study these parameters *in vivo* due to the lack of imaging tools. Here, we present luminescent biocompatible sensor foils for dual imaging of pH_e and oxygenation *in vivo*. To visualize pH_e and oxygen, we used time-domain dual lifetime referencing (tdDLR) and luminescence lifetime imaging (LLI), respectively. With these dual sensors, we discovered centripetally increasing pH_e-gradients on human chronic wound surfaces. In a therapeutic approach, we identify pH_e-gradients as pivotal governors of cell proliferation and migration, and show that these pH_e-gradients disrupt epidermal barrier repair, thus wound closure. Parallel oxygen imaging also revealed marked hypoxia, albeit with no correlating oxygen partial pressure (pO_2)-gradient. This highlights the distinct role of pH_e-gradients in perturbed healing. We also found that pH_e-gradients on chronic wounds of humans are predominantly generated via centrifugally increasing pH_e-regulatory Na^+/H^+-exchanger-1 (NHE1)-expression. We show that the modification of pH_e on chronic wound surfaces poses a promising strategy to improve healing. The study has broad implications for cell science where spatial pH_e-variations play key roles, e.g. in tumor growth. Furthermore, the novel dual sensors presented herein can be used to visualize pH_e and oxygenation in various biomedical fields.

Key words: fluorescence imaging, wound healing, cell migration, gradient sensing, proton transporters

Introduction

In multicellular organisms, acute (i.e. physiological) wound healing is a dormant mechanism to restore barrier integrity upon injury [1-3], and it comprises three major phases: (i) inflammation (e.g. leukocyte recruitment, secretion of cytokines/chemokines and growth factors), (ii) tissue formation (e.g. fibroblast and keratinocyte proliferation/migration, neoangiogenesis), and (iii) remodeling (e.g. by matrix metalloproteinases = MMPs) [1, 3-5]. In chronic wounds, however, this program prematurely stalls. Chronic wounds affect approximately 1-2% of the aging population in developed countries and thus pose an exceptional health and socio-economic issue [6]. About a third of the dermatological health budget is spent on the treatment of chronic wounds, more than for all dermato-onocological indications (melanoma and other skin cancers) taken together [6, 7].

A plethora of factors may be the starting point for chronic wound development [8, 9], yet little is known about the precise mechanisms which prevent cells from restoring an intact epithelial cover. Understanding the spatial distribution of biological parameters in healing is crucial to elucidate their impact on the cells involved in wound repair. In recent years, gradients of signaling molecules have been found to govern directional cell migration in acute wounds [8, 10-12]. In this context, the wound fluid plays a crucial role [13-16] as spatial patterns of extracellular signals therein (e.g. cytokines, chemokines, and H_2O_2) are important in regulating wound repair [8, 10, 17]. Little is known, however, about equivalent mechanisms possibly present in chronic wounds.

Extracellular hydrogen ion concentration (pH_e) is precisely regulated and potentially important in signaling within chronic wounds due to its diverse cellular effects [18-21]. Additionally, cells involved in wound closure need suffient oxygen supply for upregulated energy-consuming processes, such as proliferation, migration, and protein synthesis [19-22]. Both pO_2 and pH_e are essential metabolic parameters which affect cell proliferation and migration [22, 23].

Our venture into this study was prompted by the fact that there is no satisfactory animal model for chronic wounds, and by the lack of tools for 2D-imaging of pH_e and pO_2 *in vivo*. For these reasons, the roles of pH_e and pO_2 in chronic healing of humans have hitherto remained poorly understood. The tools available (glass electrode for pH, Clark electrode for pO_2) merely yield spot-measurements [24], and may not reveal possible spatial distribution patterns. In contrast, luminescence imaging techniques are versatile tools to analyze spatial distribution patterns of biological parameters in live organisms [10, 25-27].

To address the questions raised above, we devised a 2D luminescent dual sensor for both pH_e and pO_2 based on our previous sensor concepts [28-31]. We subsequently used this sensor to visualize pO_2- and pH_e-patterns in human chronic venous ulcers, which represent the vast majority of all chronic wounds. We then studied the impact of the detected pH_e-values on keratinocytes (which are essential for restoring an epithelial cover) in terms of proliferation, viability and migration (2D/3D wound healing assays, microfluidic cell migration assays). Additionally, proton transporter expression was investigated in biopsies from different regions in chronic wounds to elucidate how the pH_e-variations are generated.

Results

Luminescent dual sensors for imaging pO_2 and pH_e *in vivo*

To visualize 2D pO_2/pH_e-distribution *in vivo*, we devised a novel referenced luminescent dual sensor (**Fig. 1A**) based on our previous sensor concepts [30, 31]. We used palladium(II)-meso-tetraphenyl-tetrabenzoporphyrin in oxygen-permeable poly (styrene-co-acrylonitrile) microparticles (PdTPTBP-PSAN) as an oxygen probe [31, 32]. For pH_e-imaging, pH-dependent fluorescein-isothiocyanate was covalently bound to aminoethylcellulose microparticles (FITC-AC). The pH-independent reference dye ruthenium(II)-tris(4,7-diphenyl-1,10-phenanthroline) was incorporated in oxygen-impermeable polyacrylonitrile microparticles ($Ru(dpp)_3$-PAN) to prevent luminescence quenching via oxygen [30]. Microparticles were embedded in a biocompatible polyurethane hydrogel layer on transparent poly(vinylidene-chloride) (PVdC) foils to prevent dye/microparticle exposure/uptake of cells, and to create a flexible 2D sensor [30, 31]. For details, see **Materials and Methods**.

Following photoexcitation, luminescence was detected with a charge-coupled device (CCD)-camera. Signals were separated by optical filters (**Fig. 1B,C**), and by two referenced time-gated measurement schemes (**Fig. 1D,E**). Luminescence lifetime imaging (LLI) [31] of integrated signal intensities of PdTPTBP-PSAN in two time gates during emission decay (**Fig. 1D**) yielded intrinsically referenced pO_2-values (**Fig. 1F**). Time-domain dual lifetime referencing (tdDLR) of integrated signal intensities during excitation (FITC-AC and $Ru(dpp)_3$-PAN signals) and emission (only $Ru(dpp)_3$-PAN signals) was used for referenced spatial pH_e-detection (**Fig. 1E,G**) [30]. For details, see **Materials and Methods**. There was no relevant dye bleaching [30], cross-sensitivity or temperature-dependency of pO_2/pH_e-signals (**Additional**

File 1: Fig. S1).

The dual sensor described herein has a response time (99% signal intensity change) of ~1 min towards both oxygen and pH as shown in previous works on sensors for pH_e and pO_2 [28, 30, 31]. Response time is mainly determined by the diffusion of oxygen and protons through the hydrogel layer, which therefore was kept thin (6 µm) in order to warrant fast response, in particular to pH_e [28, 30, 31, 33]. It is also mandatory that sensor layers are well-conditioned (e.g. in Ringer´s solution, see **Materials and Methods**) prior to use. Oxygen diffuses quite rapidly through the PSAN copolymer microparticles, which are entirely impermeable to protons.

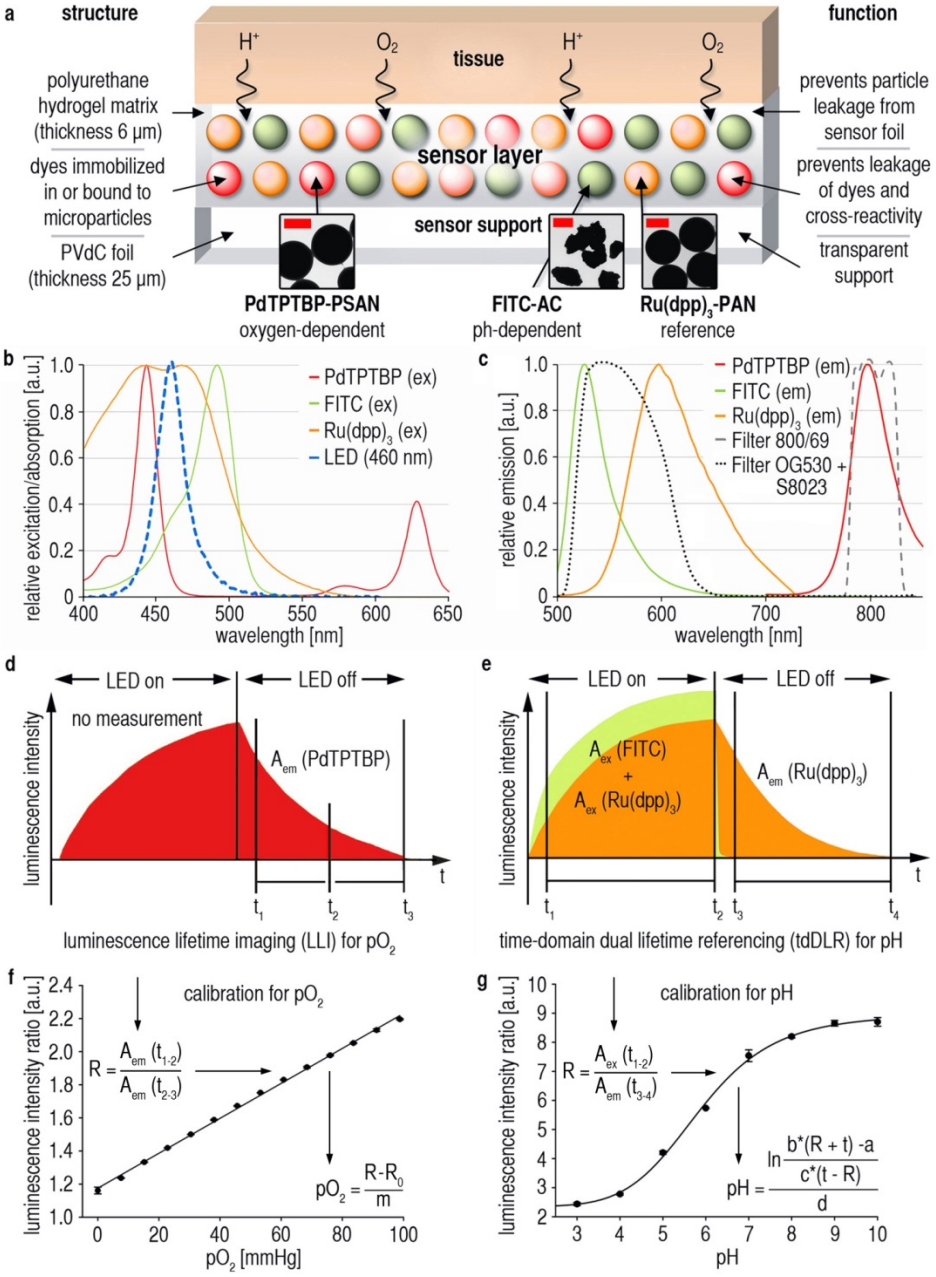

Figure 1: Dual 2D luminescence imaging of pO_2 and pH_e *in vivo*. (**A**) Sensor foil scheme: Oxygen-dependent palladium(II)-meso-tetraphenyltetrabenzoporphyrin incorporated in oxygen-permeable poly(styrene-co-acrylonitrile) particles (Pd-TPTBP-PSAN), pH-sensitive fluorescein-isothiocyanate bound to aminocellulose particles (FITC-AC), and the pH-independent reference dye ruthenium(II)-tris(4,7-diphenyl-1,10-phenanthroline) in oxygen-impermeable polyacrylonitrile particles $(Ru(dpp)_3$-PAN). Microparticles were embedded in a polyurethane hydrogel matrix on poly(vinylidene-chloride) (PVdC) foils. Dye leakage was prevented by binding the dyes to or incorporating them into microparticles. By embedding the particles in hydrogel, leakage of particles from the sensor was also prevented. The insets show transmission electron-microscopic (TEM) pictures of the sensor particles (bars are: left and right image 0.5 µm, middle image 2 µm). (**B**,**C**) Excitation (ex) (460 nm light emitting diode = LED) and emission (em) spectra of the sensor particles. Luminescence signals were optically filtered for pO_2 (800/60 filter) and pH (OG530 + S8023 filters) visualization. (**D**,**E**) Detection schemes for pO_2 and pH. Luminescene lifetime imaging (LLI) (**D**) was used for pO_2-imaging. Luminescence intensities during emission were integrated in two separate time-frames, and a ratio (*R*) of these data gives a referenced signal for pO_2. Time-domain dual lifetime referencing (tdDLR) (**E**) was used for pH-imaging. The combined signal intensities of pH-dependent FITC and pH-independent $Ru(dpp)_3$ were integrated in a time-gate during excitation, and only the long-lasting reference signal of $Ru(dpp)_3$ was detected in a time-gate during emission. The ratio (*R*) of these data gave a referenced signal for pH. (**F**,**G**) Calibration curves for pO_2 and pH. Solving the linear fit for pO_2 and the sigmoidal fit for pH enabled pO_2/pH_e-calculations for each pixel. Measured luminescence intensity ratios (*R*) obtained for each pixel were inserted in the respective equations to give referenced pO_2/pH_e-values, which displayed as pseudocolor maps to show the spatial distribution of these parameters.

The (commercially available) polyurethane hydrogel chosen here is a trade-off between diffusion rates, biocompatibility, ease of handling and optical properties. Conceivably, similar polymers may also be used: other polyurethanes, hydrogels of the polyacrylamide, silamine, or glucosamine type, and respective composites [33].

Another major concern is that horizontal analyte diffusion in the hydrogel might alter the spatial resolution over time. In previous works, we studied the spatiotemporal resolution of our sensor concept [28, 30]. This is important as two diffusion processes consistently and simultaneously occur: horizontal and vertical diffusion, both contributing to the final image. We studied the spatiotemporal resolution using continuous microscopic luminescence imaging of a drop (pH 8) on a sensor foil impregnated in a solution of pH 4. We were able to demonstrate that pH-values remain virtually unchanged over 30 min at a resolution of less than 5 µm [30]. Horizontal proton diffusion is minimal as seen in our spatiotemporal microscopic imaging experiments [30]. Similar experiments were done for pO_2, showing that oxygenation can also be visualized at high spatiotemporal resolution [28, 31].

Dual visualization of pO_2 and pH_e on human chronic wounds

In humans, the vast majority of chronic wounds are ulcers caused by chronic venous insufficiency, i.e. reduced venous backflow from the lower limbs. Long-standing ulcers with no tendency to reepithelialize were specifically chosen (**Fig. 2A**, **Additional file 1: Table S1**). Sensors were then used to visualize pO_2 and pH_e in this wound entity.

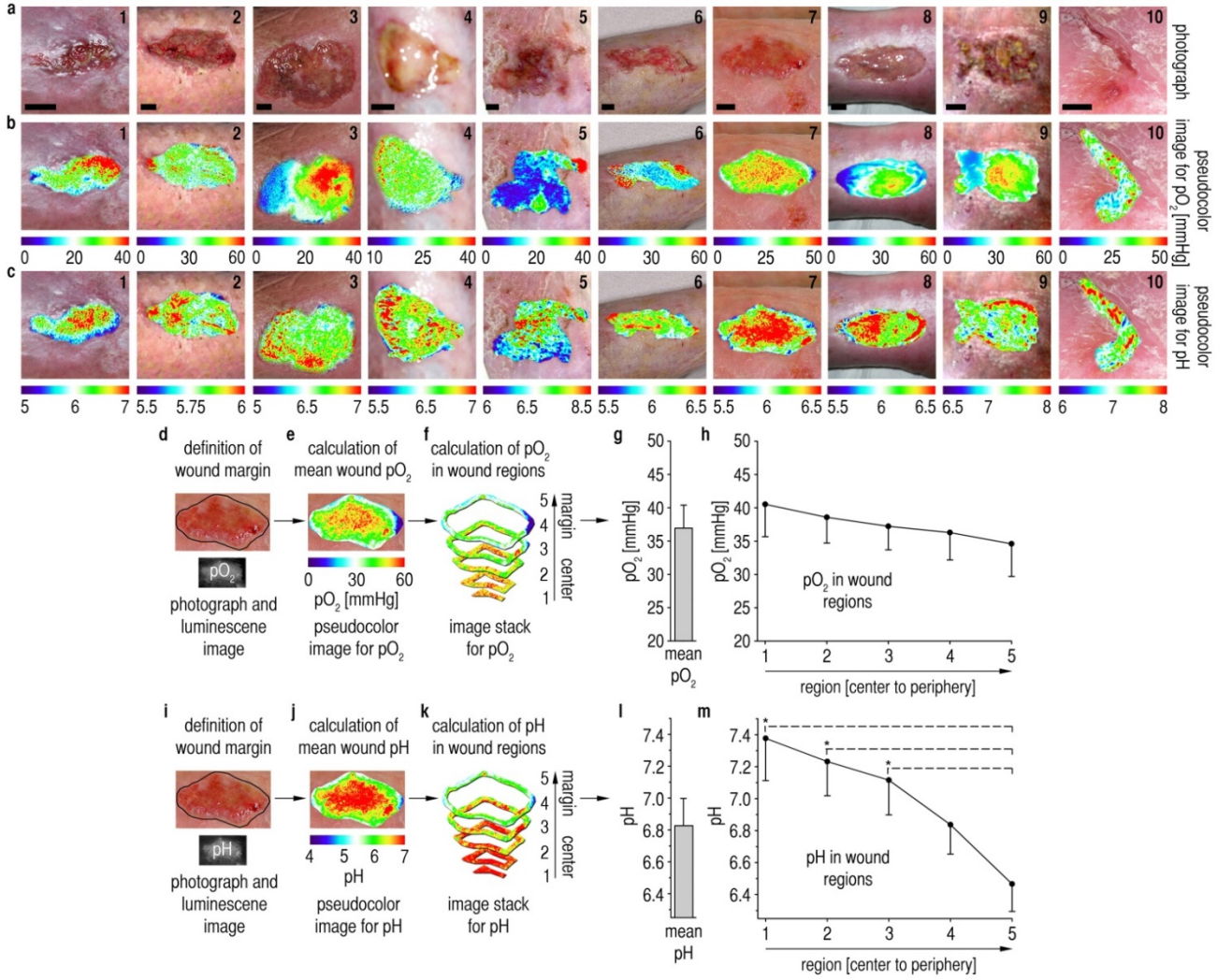

Figure 2: Spatial patterns of pO_2 and pH_e on chronic wound surfaces. (**A**) Photographs of chronic venous ulcers on the lower legs of patients. Scale bars, 1 cm. (**B**,**C**) Distribution of pH_e and pO_2 in chronic wounds. pO_2-values range from 0 up to 60 mmHg with high spatial variability. pH_e-values range from ~5 up to ~8 with high interindividual variability. In large areas, pH_e increased from the wound peripheries towards the wound centers. (**D**,**I**) After defining the wound margins, mean pO_2/pH_e for the entire wound surface was calculated (**E**,**J**,**G**,**L**). (**F**,**K**) Self-programmed computerized macros (**Materials and Methods**, **Macro S1**) served to obtain pO_2/pH_e-data for the different wound regions. (**G**,**L**) Mean pO_2 amounted to ~37 mmHg for the entire wound surface, and mean pH_e was ~6.8. (**H**) A relatively homogenous distribution of pO_2-values was found when analyzing data from all wound regions. (**M**) There were significant differences in pH_e-values between the wound periphery and regions in the wound center. A pH_e-gradient was found, starting with high mean pH_e in the wound center (~7.4) and decreasing to low pH_e near the wound margins (~6.5). n = 10, mean ± s.e.m., one-way ANOVA $p<0.001$, *$p<0.05$ in post-hoc Tukey-tests.

It shall be noted here that the formation of air bubbles between sensor and tissue (when depositing the sensor film on the wound) is detrimental because it causes undesired effects: a delayed response to oxygen, a lack of response to pH (which is water-bound), and the formation of a reservoir for oxygen which heavily biases accuracy. Therefore, sensors were gently applied to wounds starting from one wound edge and were allowed to slowly adhere to the tissue surface by adhesion forces. The wound fluid, even if minimal, consistently allowed the foils to adhere to the wound surface. Foils were then photoexcited with LEDs, and respective time-gated luminescence signals for pO_2/pH_e were optically filtered and recorded with a CCD-camera using 2D-LLI/2D-tdDLR. We processed images with ImageJ to yield 2D pseudocolor maps of pO_2/pH_e in chronic wounds (**Fig. 2B,C**).

To analyze 2D distribution of pO_2 and pH_e, we developed computerized macros (**Additional file 5: Macro S1**), capable of dividing imaging data from asymmetrical wound surfaces in 5 annular regions, each resulting from the percental distance (necessary for different wound sizes) from the wound margin. After marking the wound margins in the photographs (**Fig. 2D,I**), these contours were transfered to luminescence images, and these images were subsequently divided into annular regions (**Fig. 2E,F,J,K**). Mean pO_2/pH_e was calculated for each region per wound from all values found in these regions. Additionally, mean pO_2/pH_e was calculated for each entire wound from all values within the margins. For details on image processing, see **Materials and Methods**.

Chronic wound surfaces were hypoxic at ~37 mmHg, with a mean pH_e of ~6.8 (**Fig. 2G**,**L**), even though the epidermal barrier was absent in most areas. We have previously shown that one day after wounding pH_e is above 8 and pO_2 is ~60 mmHg, and that both parameters decrease during epidermal barrier restoration in physiological healing [30, 31]. Surprisingly, we found centripetally rising pH_e-values in chronic wounds (**Fig. 2M**). Despite a high variability between the wounds in terms of size, shape and overall level of pH_e, vast areas with centripetally rising pH_e-values were found in the wounds. Mean pH_e-values were significantly higher with increasing distance from the margins (periphery-pH_e ~6.5, center-pH_e ~7.4). No corresponding pO_2-gradient (**Fig. 2H**) was observed, highlighting the fact that the pH_e-gradient is not merely caused by the lack of a functional epidermal barrier. The degree of wound hypoxia measured here has been shown to critically impair keratinocyte proliferation and migration in healing [20, 22, 34-36].

pH_e-gradients and epidermal barrier repair - a therapeutic approach

We then studied the functional impact of the observed pH_e-variations on epidermal barrier repair. Using pH-adjusted culture media (**Additional File 1: Fig. S2**), we first investigated pH_e-effects on cell proliferation. With ^{3}H-methyl-thymidine uptake as a marker for proliferation, we found a marked reduction of keratinocyte proliferation at the low pH_e-values found at the wound periphery when compared to the high pH_e at the wound center (**Fig. 3A**). Moreover, we found that cell viability, as measured via ATP-bioluminescence assays, was critically reduced at the pH_e-values found at the outer wound regions (**Fig. 3B**) as compared to the cell viability at the pH_e found at the wound center. WST-1 tests confirmed a rise in cell viability with increasing pH_e (**Additional File 1: Fig. S3**). Therefore, keratinocyte proliferation and viability are reduced at the pH_e found at chronic wound peripheries.

Next, we studied how cell migration is affected by the pH_e-values found in chronic wounds using 2D wound healing scratch assays (**Fig. 3C**) [37]. We demonstrated that gap closure of keratinocyte epithelial monolayers is impeded by low pH_e-values (6-6.5), whilst with rising pH_e-values (7-7.5) the injured monolayer closed completely after 48 h.

To further investigate the effect of pH_e on multilayered epithelia, we designed 3D skin constructs using keratinocyte/fibroblast co-culture. After wounding, a thin layer of pH-adjusted media (pH_e 6.5 or 7.4), which served as a surrogate for the wound fluid, was pipetted onto injury sites in 3D skin constructs. Two days after wounding, histological evaluation revealed a multilayered epithelium on injury sites with pH_e 7.4 media, which covered the entire wound area (**Fig. 3D**). No wound closure was observed in the wound models with pH_e 6.5 media (**Fig. 3D**), demonstrating that low pH_e inhibits multilayer epidermal repair, thus wound closure.

To elucidate how pH_e-gradients influence keratinocyte migration at the single-cell level, we devised a microfluidic cell migration assay [38]. The pH_e-gradients were established within the pH_e-range measured *in vivo* (**Fig. 3E**, **Additional File 1: Fig. S4**). In this microfluidic assay, we observed that keratinocyte motility was lower at a pH_e of ~6.4 as compared to higher pH_e-values of ~6.8 and ~7.2 (**Fig. 3 F-H**, **Additional File 1: Fig. S5**, **Movies S1-3**). The migration velocity of keratinocytes increased significantly at higher pH_e-values (**Fig. 3I,J**). Furthermore, the y forward migration index (yFMI) indicated that keratinocytes at low pH_e of ~6.4 exhibit a low tendency to migrate towards higher pH_e (**Fig. 3K,L**). yFMI of keratinocytes was highest at pH_e ~6.8 (addi-

tional information on accumulated distance and endpoint y in **Additional File 1: Fig. S6**). As keratinocyte proliferation, viability, migration velocity, and the respective yFMI are critically reduced at the low pH_e found at the wound periphery, keratinocytes may not be sufficiently recruited from the wound margins to restore an intact epidermal barrier.

Furthermore, we found that keratinocytes cultured at the predominantly high pH_e at wound centers secreted markedly more IL-6 and IL-8 (important direct and indirect mediators of keratinocyte proliferation and migration) [39, 40] when compared with those at lower pH_e as found at the wound periphery (**Fig. 3M**, **Additional File 1: Fig. S7**).

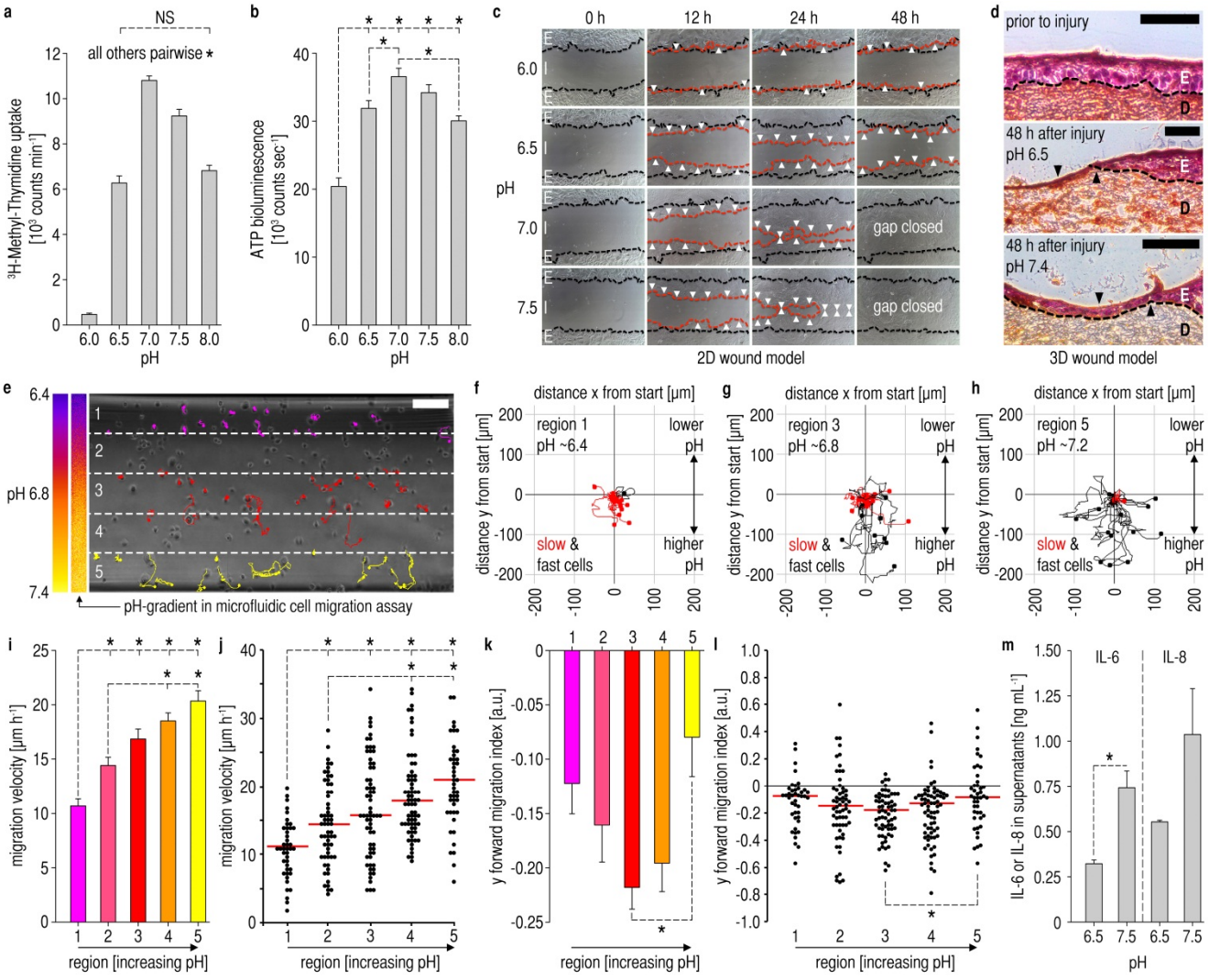

Figure 3: Impact of pH_e on epidermal barrier repair. All experiments: human epidermal keratinocytes (HK), (**A**,**B**,**I**,**K**,**M**) mean ± s.e.m. (**A**,**B**) Proliferation and viability (also see **Additional File 1: Fig. S3**) of HK was significantly reduced at low pH_e-values. n = 12, NS = not significant, one-way ANOVA $p<0.001$ and *$p<0.05$ in post-hoc Holm-Sidak test. (**C**) In a 2D scratch assay, there was almost no movement of the HK monolayer at low pH_e of 6.0, whereas with rising pH_e centripetal monolayer movement increased. Black dashed lines = migration front after injury, red dashed lines = migration front after the respective time, white arrows = regions of significant migration. E = epithelium, I = injury, n = 3. (**D**) 3D Skin constructs of co-cultured HK and fibroblasts. After mechanical injury, healing was studied with pH-adjusted media (as substitutes for the wound fluid) at the injury site. No healing was observed at low pH_e 6.5 after 48 h, whereas at pH_e 7.4 the wound was covered with a multilayered epithelium. Scale bars, 200 µm, D/E = dermis/epidermis equivalent, n = 3. (**E**) Chamber of a microfluidic cell migration assay. Pseudocolor scale and actual pH_e-gradient (horizontally downscaled to show the gradient over the entire chamber) in the microfluidic chamber (visualization via luminescent BCECF). Numbers 1-5 denote regions for further analyses. HK (at 0 h) and according migration traces (colored) within 16 h are shown. Scale bar, 200 µm. (**F**-**H**) Trajectory lines of HK superimposed on coordinates (start at x/y = 0 µm). Mean slow cell velocity ≤ 12.6 µm/h, mean fast cell velocity > 12.6 µm/h. At low pH_e, nearly all cells exhibited slow movement, whereas migration distance and the proportion of fast cells increased with rising pH_e (**E**-**H**, results from one representative experiment, additional experiments/videos: **Additional File 1: Fig. S5**, **Movies S1-3**). n = 3 experiments. (**I**-**L**) Results from three microfluidic assays. Migration velocity (**I**) increased with rising pH_e. The corresponding scatter point plot (**J**) shows results for all cells (red lines = medians). (**K**,**L**) y forward migration index (yFMI) was low at pH_e ~6.4, and highest at pH_e ~6.8. (**L**) red lines = medians. Together with velocity results, this demonstrated minimal chemotactic/migration activity at low pH_e as found at wound peripheries. Cells tracked in 3 experiments: region 1 (n = 42), 2 (n = 60), 3 (n = 65), 4 (n = 69), 5 (n = 44). a.u. = arbitrary units, one-way ANOVA on ranks $p<0.001$ and *$p<0.05$ in post-hoc Dunn´s test. (**M**) Secretion of mediators of proliferation/migration, namely IL-6 and IL-8, is markedly increased at high pH_e (see **Additional File 1: Fig. S7**). n = 3, one-way ANOVA $p<0.001$ and *$p<0.05$ in post-hoc Tukey test.

Proton transporter expression in chronic wounds

To decipher how the pH_e-gradients in chronic wounds might arise, we studied the expression levels of essential pH_e-regulatory ion transporters in punch biopsies from human wounds (**Additional file 1: Table S2**). We assessed the protein expression level of Na^+/H^+-exchanger-1 (NHE1), a ubiquitously expressed transporter which is highly regulated (e.g. by cytokines, H_2O_2, reduced intracellular pH) [41, 42], and which contributes importantly to the development of acidic pH_e, e.g. in carcinomas [41, 43, 44]. Immunofluorescence analysis of NHE1 in sections from intact skin, wound peripheries and centers (**Fig. 4A**,**B**, **Additional File 1: Fig. S8**) revealed an increase in total and plasma membrane NHE1-density at wound peripheries, yet not at the central wound region, when compared with surrounding intact tissue. In the core of the wound, NHE1 protein-expression seemed to decrease strongly again, reaching a level similar to that in the normal tissue. For validation, quantitative reverse transcription PCR (qRT-PCR) for NHE1 was done (**Fig. 4C**), demonstrating a similar pattern of mRNA-expression, with greatly increased NHE1-mRNA-levels at the wound periphery, decreasing again at the wound center. Western blots confirmed the presence of a single band of the correct size for each transporter.

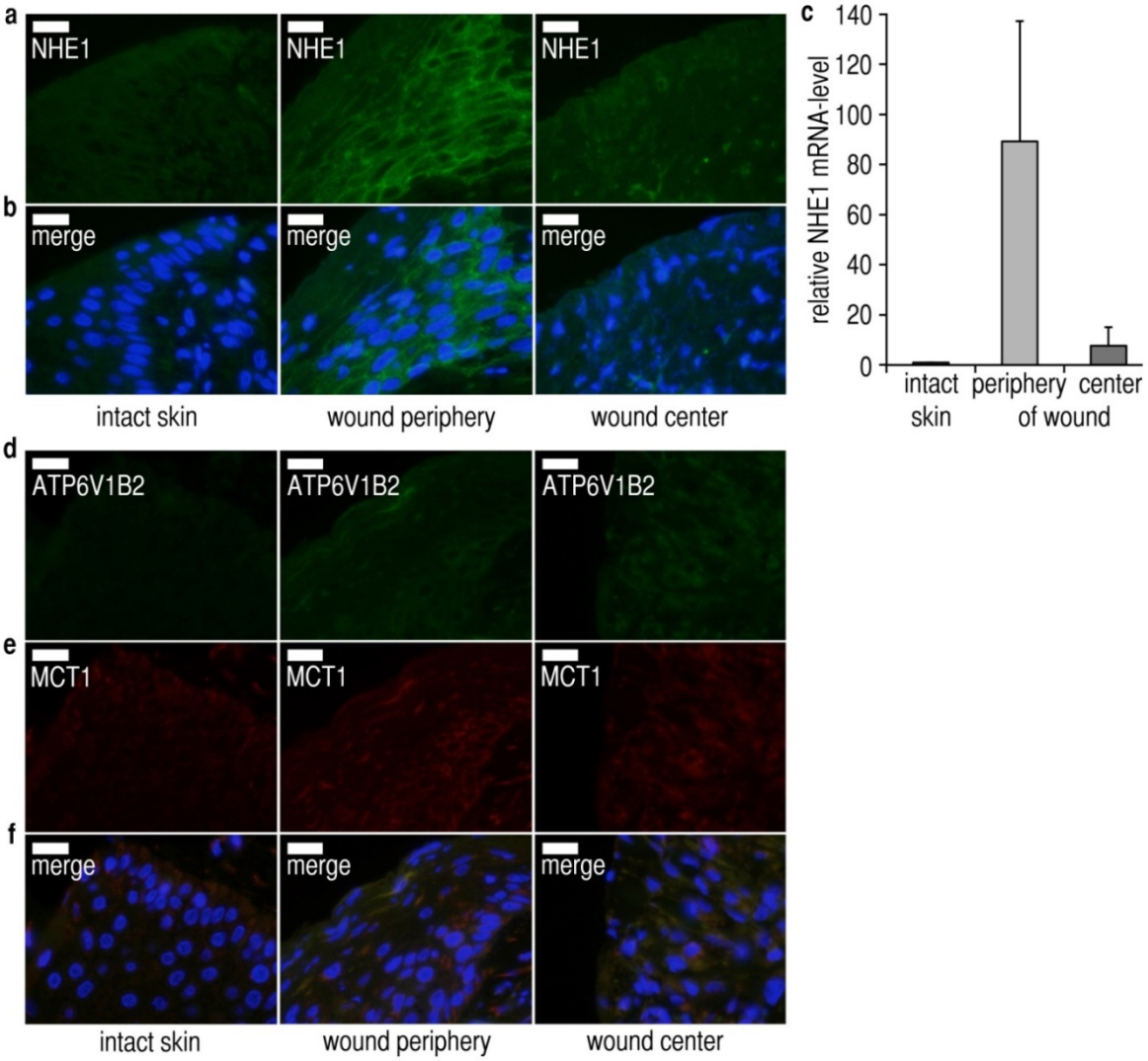

Figure 4: Expression and localization of pH_e-regulatory proton transporters in chronic wounds. (A-F) Three biopsies (adjacent intact skin, wound periphery, wound center) were taken from each patient (n = 3) and analyzed for proton transporter expression. The immunofluorescence images shown are representative of at least three different sets of images from each wound region. Sections were counterstained with DAPI (blue) for nuclei staining. Scale bars, 20 µm. (**A-C**) Representative (**A,B**) immunofluorescence staining and (**C**) quantitative reverse transcription PCR (qRT-PCR) of Na^+/H^+ exchanger-1 (NHE1) from adjacent intact skin, peripheral and central wound tissues from chronic wound patients. (**A,B**) NHE1-expression is strongly upregulated in peripheral wound tissue, but not in the central part of the wound. NHE1-antibodies were tested in Western blotting and found to produce bands of the correct size. Additional immunofluorescence images are shown in **Additional File 1: Fig. S8**. (**C**) mRNA of NHE1 was extracted from adjacent normal tissue, the wound peripheries and wound centers. We found that NHE1-mRNA was strongly upregulated at the wound periphery as compared to intact skin and the wound center. Mean ± s.e.m., n = 3. (**D-F**) The expression levels of the (**D**) plasma membrane vacuolar-type ATPases subunit B2 (ATP6V1B2) and the (**E**) (H^+-lactate) monocarboxylate cotransporter 1 (MCT1) were not significantly upregulated in the peripheral and central wound sections as compared to intact skin. Additional immunofluorescence images are shown in **Additional File 1: Fig. S9**. Taken together, these results show that NHE1-levels are centrifugally upregulated in chronic wounds, and suggest that increased NHE1-mediated hydrogen ion extrusion acidifies the wound fluid with increasing distance from the center.

To assess whether other pH_e-regulatory transporters might exhibit similar gradients of expression, we performed immunofluorescence analysis for the (H^+-lactate) monocarboxylate transporter 1 (MCT1), and for the vacuolar ATPase subunit B2 (ATP6V1B2). The protein levels of both transporters were virtually identical in intact skin, wound peripheries and wound centers (**Fig. 4D-F**, **Additional File 1: Fig. S9**). Taken together, these data are highly consistent with the observed pH_e-gradient: NHE1-expression is upregulated at the wound periphery, and increased NHE1-mediated hydrogen ion extrusion acidifies the wound fluid with increasing distance from the center. It is, however, impossible to add an NHE1-inhibitor (e.g. 5´N-ethylisopropylamiloride = EIPA, cariporide) prior to measurements on humans to block NHE1-mediated acidification of the wound fluid.

Discussion

Gradient sensing is an essential biological mechanism governing directional cell migration in both prokaryote and eukaryote cells [45-50]. In physiological wound healing, gradients of growth factors (e.g. EGF) [8, 11], cytokines and chemokines [8], or small signaling molecules (e.g. H_2O_2) [10] have been shown to be decisive cues in mediating barrier repair.

In this study, we showed that gradients of extracellular hydrogen ion concentrations exist on the surface of chronic wounds, and that these pH_e-gradients negatively affect keratinocyte viability, proliferation and migration at the wound periphery. Decreasing acidity towards the wound center inhibits centripetal keratinocyte recruitment, thus preventing wound closure as shown in 2D and 3D wound healing assays as well as in microfluidic cell migration experiments (scheme in **Additional File 1: Fig. S10**).

It has been reported recently for $\alpha_v\beta_3$ CHO-B2 cells and microvascular endothelial cells, that low pH_e leads to increased integrin $\alpha_v\beta_3$-expression and subsequently reduced cell migration velocity [51, 52]. Based on our findings, this means that, at the wound periphery, these cells would be less motile and more prone to maintain their adherence, exactly at the region from which they are recruited from for healing.

We also detected high levels of direct and indirect mediators of keratinocyte proliferation and migration, namely IL-6 and IL-8 [39, 40], at the pH_e found at the wound center (**Additional File 1: Fig. S7**). In contrast, keratinocytes secreted low amounts of IL-6 and IL-8 at the low pH_e-values found at the wound periphery, which may also contribute to reduced centripetal keratinocyte recruitment. Another interesting finding was that interferon-γ (INFγ) release from keratinocytes increased with rising pH_e (**Additional File 1: Fig. S7**). INFγ is known to stimulate VEGF production of keratinocytes [53], and VEGF is a key molecule in neoangiogenesis during healing. However, at the low pH_e as found at the wound periphery, we found low levels of INFγ in keratinocyte supernatants. Therefore, the pH_e-gradients found are possibly detrimental for neoangiogenesis at the wound periphery. More experiments have to be done to study the effects of the pH_e-generated cytokine and chemokine secretion patterns on cell migration and proliferation. Additionally, the activity of MMPs involved in healing [5] is regulated by pH_e, and it has yet to be shown how the varying pH_e-values reported here affect these enzymes in the different wound regions.

Next, we showed that the pH_e-gradients found on chronic wound surfaces are predominantly generated via centrifugally increasing NHE1-expression. NHE1-expression is strongly upregulated at the wound periphery, and increased NHE1-mediated hydrogen ion extrusion acidifies the wound fluid in this region. Other acid extruding transporters, such as MCT1 and vacuolar type H^+-ATPases, were not significantly upregulated at the wound periphery. The immunofluorescence and qRT-PCR data in conjunction with the measured pH_e-gradients suggest that NHE1 is predominant, in accordance with its major physiological roles in acid extrusion. It is obviously impossible to add an NHE1-inhibitor (EIPA or cariporide) prior to measurements on humans. As NHE1 is the only NHE-isoform found in keratinocytes and epidermis [54], no other isoforms are relevant here. With respect to MCT-isoforms, no studies exist specifically addressing their roles in keratinocytes/epidermis. MCT1 is, however, the most widespread isoform, with MCT2, 3, and 4 showing much more restricted expression patterns. MCT2-expression is very low in human tissues (with the exception of testis), MCT3 is restricted to retina and the choroid plexus, and MCT4-expression is generally limited to tissues which use glycolysis for their energy metabolism (e.g. white skeletal muscle fibers, astrocytes, white blood cells, chondrocytes, certain tumor cells, cells under severe hypoxia) [55]. Therefore, it can be concluded that no other NHEs than NHE1 contribute to the pH_e-gradient, and that a major contribution from MCT2-4 seems very unlikely.

Further, we describe, for the first time, the visualization of chronic wound oxygenation, and we found marked hypoxia (~37 mmHg), albeit with no correlating pO_2-gradient. During physiological healing, we have previously shown that pO_2 amounts to ~60 mmHg on the first day after epidermal barrier removal, and that pO_2 gradually decreases during epidermal barrier recovery [31]. Interestingly, pO_2 in chronic wounds is markedly lower, despite the lack of

epidermal coverage. Such low pO_2-values critically impair keratinocyte proliferation [19, 20, 36] (partially by miRNA 210 upregulation) [34] and protein synthesis (e.g. cytokines, chemokines, growth factors), both processes being prerequisites for healing. Recently, it was also shown that hypoxia may partially arrest the cell cycle in keratinocytes via hypoxia inducible factor-1α (HIF-1α), which leads to miRNA 210-induced silencing of the transcription factor E2F3. HIF-1α is, however, also crucial for keratinocyte migration via regulation of laminin-332 [35]. Other effects of hypoxia are mediated by miRNA 21, which silences early growth response factor 3 (EGR3). According to the literature [19], the pO_2 of ~37 mmHg measured in this study may reduce keratinocyte proliferation by ~60% when compared to normoxic conditions. Hypoxia has, however, also been reported to be a stimulus for keratinocyte migration, yet most patients with chronic wounds are of advanced age, and it is known that hypoxia loses its potential as a stimulus for cell migration with increasing patient age [21, 56]. Therefore, we conclude that the low pO_2-values we measured on chronic wound surfaces contribute to reduced keratinocyte proliferation and migration, thus impairing barrier rapair. Other miRNAs, such as miRNA-198, have recently been shown to be decisive factors in chronic wound healing [57].

In summary, we present the first observation of presumably NHE1-generated pH_e-gradients on chronic wounds. We further provide unique evidence for the notion that pH_e-gradients inhibit keratinocyte supply from the wound margins in chronic wounds (**Additional File 1: Fig. S10**), a previously undescribed pathomechanism. Modulating pH_e in chronic wounds poses a promising and feasible strategy for future therapeutics (e.g. dynamic hydrogels) [58] to improve patient outcomes. Hydrogels which restore a higher pH_e in chronic wounds, especially at the periphery, might stimulate increased proliferation and centripetal migration of keratinocytes. pH-gradients also play an important role in tumor metabolism [43, 44], and therefore these findings provide evidence for a novel link between cancer and wounds in terms of pH_e-regulated cell proliferation and migration [59]. In humans, there are four proton-sensing G protein-coupled receptors (GPCRs), which are possibly involved in sensing the above-mentioned pH_e-gradients: G2A (GPR132), GPR4, OGR1 (GPR68), and TDAG8 (GPR65) [60, 61]. These GPCRs are mainly activated when pH_e drops below the physiological range, i.e. at the pH_e-values we found at the wound periphery. Further studies should elucidate the role of proton sensing GPCRs in pH_e-dependent cell proliferation and migration in wounds and tumors [43, 44, 59, 62].

Materials and methods

Luminescent Microparticles

The oxygen probe PdTPTBP (λ_{ex} 444 nm, λ_{em} 797 nm, lifetime 50-300 µs depending on pO_2, Sigma-Aldrich, Seelze, Germany) was incorporated into oxygen-permeable PSAN (30 wt% acrylonitrile content, M_w 185,000, Sigma-Aldrich) in a 1/50 ratio to form oxygen sensor beads (PdTPTBP-PSAN, diameter 0.5-1 µm). Polymer and dye were dissolved in dimethylformamide (0.12 mL per mg net weight, 60 °C). After cooling the mix to room temperature, particles precipitated under stirring (350 rpm) with the addition of distilled water (0.32 mL per mg net weight, drop-wise, 1 mL s^{-1}). The solution was stirred for 30 minutes to ensure complete precipitation. The reaction can be scaled up to generate 250 mg of polymer. Particles were washed (6 x with ethanol, 8 x with distilled water), and filtered via centrifugation (10 min, 1,030 x g) after each washing step. Reactions were conducted at room temperature unless otherwise stated and particles were freeze-dried for storage (Modulyo, IMA Edwards, Bologna, Italy).

pH-dependent FITC (λ_{ex} 495 nm, λ_{em} 525 nm, lifetime < 5 ns, Sigma-Aldrich) was conjugated to AC particles (PreSens, Regensburg, Germany) in a 1/50 wt/wt ratio in sodium bicarbonate buffer (50 mM, pH 9, 1.8 mL per mg FITC) to form FITC-AC particles (2 h reaction time, diameter 0.75-3 µm). Residual amino groups on the particle surface were blocked with acetic anhydride (Sigma-Aldrich). FITC-AC was reacted with acetic anhydride and ethanol in a 1/2 wt/wt ratio (0.1 mL per mg AC, 12 h reaction time). Particles were washed (8 x with distilled water), and filtered via centrifugation (10 min, 1,030 x g, EDA12, Hettich, Tuttlingen, Germany) after each washing step.

$Ru(dpp)_3$ (λ_{ex} 441 nm, λ_{em} 597 nm, lifetime ~6 µs, Sigma-Aldrich) was incorporated in PAN (Sigma-Aldrich) at a 1/50 ratio to form $Ru(dpp)_3$-PAN particles (diameter 0.5-1 µm). Particles were formed by precipitating dye and polymer dissolved in dimethylformamide (0.2 mL per mg net weight) with distilled water (0.28 mL per mg net weight, drop-wise addition, 1 mL s^{-1}) and the subsequent addition of Brine (0.08 mL per mg net weight). The reaction can be scaled up to 250 mg of polymer. Particles were washed (8 x with distilled water, 4 x with ethanol), and filtered after each washing step via centrifugation (10 min, 1,030 x g).

Particle sizes were assessed with a LEO912 AB transmission electron microscope (Carl Zeiss, Oberkochen, Germany). The microparticle design effi-

ciently prevents Förster resonance energy transfer (FRET).

Sensor Foils

The microparticles (PdTPTBP-PSAN, FITC-AC, $Ru(dpp)_3$-PAN) were mixed (ratio 2/3/1). The particle mix was dispersed (15 mg mL^{-1}) in hydrogel solution consisting of 5% wt/vol polyurethane hydrogel (type D4, Cardiotech International Inc., Plymouth, MN, USA) in ethanol/water (90/10 vol/vol). This mixture was spread on a transparent PVdC-foil (thickness 25 µm, Saran plastic wrap, S.C. Johnson & Son Inc., Racine, WI) with a knife-coating device (K Control Coater model 101, RK Print-Coat Instruments Ltd., Litlington, UK) to form a 120-µm-thick film (**Fig. 1A**). After drying, sensor layer thickness was 6 µm. One mL of sensor mix generates a sensor film of 83 cm^2.

Luminescence Imaging

Imaging for pO_2/pH_e was undertaken using a time-gated imaging setup (ImageX TGI System, Photonic Research Systems, Newhaven, UK) with an integrated 12-bit CCD chip (640 x 480 pixels). The camera was combined with an array of light emitting diodes (LED, λ = 460 nm, Luxeon V Star LXHL-LB5C 5W, Philips Lumileds Lighting Company, San Jose, CA, USA) equipped with a FITC excitation filter (Chroma Optical, Brattleboro, VT, USA) (**Fig. 1B**).

The LLI-scheme (**Fig. 1D,F**) was used for pO_2-imaging (parameters: subtract background, 70 µs gate width, 1 µs delay time for window 1 and 36 µs delay time for window 2, 500 µs lamp pulse, 400 Hz recording frequency, 2 s integration time). An 800/60 nm bandpass filter (Omega Optical, Brattleboro, VT, USA) served to separate emitted oxygen probe luminescence from background and pH_e-dependent signals (**Fig. 1C**). Triplicates of each image were collected in every measurement cycle.

The tdDLR-scheme (**Fig. 1E,G**) was used for imaging pH_e-distribution (parameters: subtract background, 5 µs gate-width, 5.5 µs delay time for gate 1, 0.25 µs delay time for gate 2, 6 µs lamp pulse, 400 Hz recording frequency, 100 ms integration time). The glass filters OG530 and S8023 (Schott, Mainz, Germany) were used as emission filters (**Fig. 1C**). Triplicates of each image were recorded in each measurement cycle.

Study Subjects

Participants were provided with verbal and written information on the study, and signed informed consent was obtained from each participant. The local ethics committee gave approval (University Medical Center Regensburg, No. 06/171: 2007), and experiments were conducted in accordance with the current revision of the Declaration of Helsinki. Impaired blood circulation (venous backflow, arterial inflow, microcirculation) is often a precursor to the development of chronic wounds. Study subjects were included based on the main causative disease being venous insufficiency, one wound diameter being at least 3 cm (for adequte analysis of signal distribution in an *in vivo* setting), and the absence of any healing tendency.

In Vivo Imaging

Sensor foils were preconditioned (30 min, room temperature) in Ringer´s solution (B. Braun Melsungen, Melsungen, Germany) before use. Sensors were gently applied to the wound surface starting from one margin of the wound. Adhesion forces enabled the foils to adapt to tissue surfaces. The formation of air bubbles between sensor and tissue was thereby prevented and uniform contact ensured. We applied no pressure to the foils during measurements. The sensors remained on the wounds for 5-10 minutes and covered the entire wound surface and parts of the surrounding tissue. The distance between sensor and camera was focus-controlled (25 cm). All images were recorded >1 min after sensor application to yield sufficient sensor response (oxygen and proton diffusion). After recording oxygen images, the filters of the camera were changed and pH_e-measurements were performed.

Image Processing

For pO_2/pH_e raw data processing, integrated luminescence intensities in gate 1 were divided by the according intensities in gate 2 (ImageX software, provided with the TGI camera system, Photonic Research Systems). pO_2/pH_e raw data were stored as 16-bit black-and-white pictures (TIFF-format).

The following processing steps were performed for each wound with Photoshop CS4 (Adobe Systems, San Jose, CA, USA): pO_2/pH_e raw data and a photograph of the wound were imported into one 16-bit PSD-file. The original wound picture was converted to grayscale and then duplicated. Layers were renamed: "Pseudocolor pH", "Pseudocolor pO2", "Photo", and "Original". "Pseudocolor pH" and "Pseudocolor pO2" were superimposed onto the identical real-color wound pictures ("Photo" and "Original") using the transformation tool. The wound margins were defined in the "Photo" layers, and regions outside the respective margins were erased. The layer "Photo" was selected and the action "macro for preparation" (**Macro S1**) was started. Thereby, the size of the image was adapted and standardized, and the defined wound area was transferred to the raw data pictures. Subsequently, the pellucid region of the

layer "Photo" was selected ("magic wand tool") and the action "macro for slicing" (**Macro S1**) was executed. During this action, raw data were sliced into five consecutive regions, starting from the wound periphery towards the center. Next, the layer "Pseudocolor pH" was selected and the action "macro for measurement" (**Macro S1**) was executed.

The grayscale mean value of the pH_e/pO_2-images from the total wound surface as well as from each slice were recorded using the "measurement tool". The "measurement log" that buffers the data was exported to a CSV-file and imported into Excel (Microsoft, Redmond, WA, USA). The imported CSV-data were multiplied by a factor of 0.0022 for re-conversion to raw data values. These values were converted to respective pO_2/pH_e-values via the calibration equations (**Fig. 1F**,**G)**.

Pseudocolor image processing was done with ImageJ (http://rsbweb.nih.gov/ij/). For illustration purposes, pseudocolor maps for pO_2/pH_e on wound surfaces were superimposed to photographs using Adobe Photoshop (**Fig. 2A-C**).

Keratinocyte culture for proliferation and viability

For ^{3}H-methyl-thymidine uptake and ATP-bioluminescence assays, primary human keratinocytes were isolated and cultured as described previously [63]. Discarded skin was obtained during routine surgical procedures (UK NRES approval: 06/Q1907/81) with the patients´ informed consent. The epidermis and dermis were separated by digestion with 4 mg ml^{-1} dispase (10 min, Invitrogen, Life Technologies Ltd., Paisley, UK) prior to liberation of keratinocytes from the epidermis by incubation with 0.5% trypsin (30 min, Invitrogen). Isolated keratinocytes were co-cultured with a feeder-layer of lethally irradiated 3T3-cells in standard Rheinwald and Green media (R&G) comprising DMEM and Ham's F12 medium (Invitrogen) at a 3:1 ratio, supplemented with 10% FCS (Gibco, Life Technologies Ltd., Paisley, UK), 10 ng mL^{-1} human recombinant EGF (Invitrogen), 10 nM cholera toxin (Sigma Aldrich, Gillingham, UK) and 0.4 mg mL^{-1} hydrocortisone (Sigma-Aldrich, UK).

For water-soluble tetrazolium-tests (WST-1), adult human epidermal keratinocytes (HEKa, Gibco) were cultured in EpiLife medium supplemented with human keratinocyte growth supplement (HKGS, Gibco) and a Pen/Strep solution in a humidified atmosphere (37°C, 5% CO_2). After reaching sub-confluency, cells were passaged using a 0.25% trypsin solution. For viability assessment and 2D migration assays, cells in passage 3 were used.

pH-adjusted media

In order to maintain experimentally induced variations in pH_e, we modified R&G media such that DMEM was substituted with Hank´s buffered M199 media (Invitrogen) with reduced bicarbonate. Whilst maintaining a similar salt concentration, this substitution allowed a range of pH_e to be stably maintained in ambient CO_2 (also see **Additional File 1: Fig. S2**). Media was adjusted to pH 6, 6.5, 7, 7.5 and 8 with the dropwise addition of 1M HCl or 2M NaOH.

^{3}H-methyl-thymidine uptake, ATP-assays and WST-1 tests

Keratinocyte proliferation was assessed using a tritiated thymidine uptake assay. Cultured keratinocytes were seeded and exposed to pH-adjusted media as above. Keratinocytes were incubated with 0.5 µCi well^{-1} ^{3}H-Methyl-thymidine (PerkinElmer, Beaconsfield, UK) for a further 24 hours, lysed using 0.1% SDS and 0.1 M NaOH, harvested onto a filter mat using a Filtermate cell harvester (PerkinElmer, UK), and radioactivity was measured using a MicroBeta counter (PerkinElmer, UK) following the addition of scintillant.

Keratinocyte viability after 24 hours at pH_e 6, 6.5, 7, 7.5 and 8 (n = 12 each) was measured using an ATP-assay. Keratinocytes were seeded into 96-well plates (5,000 cells well^{-1}) and allowed to attach for 24 hours in standard R&G growth media before removing the media and washing off any unattached cells. Cells were incubated for 24 hours in pH-adjusted media at ambient CO_2 prior to measurement of ATP-activity using an ATPlite-assay (PerkinElmer) and measurement of luminescence using a MicroBeta-counter (PerkinElmer).

Cell vitality was additionally assessed with the WST-1 cell proliferation reagent (Roche, Mannheim, Germany). Viable cells reduce the WST-1 reagent to a water-soluble formazan dye. The absorbance at 450 nm correlates to the vitality of the cells. Briefly, adult human keratinocytes (5,000 cells cm^{-2}, passage 3) were seeded in 96-well plates. After 24 hours, the medium was changed to the pH-adjusted media and cells were incubated for 24 or 48 h, respectively. Subsequently, WST-reagent was added to the wells for two hours and the absorbance at 450 nm was measured using a TECAN infinite F200 plate reader (TECAN, Crailsheim, Germany). Experiments were undertaken with six replicates per treatment.

2D and 3D wound healing models

For 2D wound healing assays, wells of a 24-well plate were incubated with 500 µl of a 10 µg ml^{-1} fibronectin/PBS (Sigma-Aldrich) solution (10 µg cm^{-2}) overnight. Afterwards, adult human keratinocytes

(passage 3) were seeded into wells (5,000 cells cm^{-2}). At confluency, we scratched the cell monolayer using a pipette tip and the medium was changed to the pH-adjusted media. Pictures of the monolayer movement were taken after 0, 12, 24, and 48 h. Experiments were undertaken in triplicate.

For 3D wound healing assays, fibroblasts, FCS and bovine collagen I (Nutacon, Leimuiden, Netherlands) were brought to neutral pH and poured into 3D culture filter inserts for 6-well plates with a growth area of 4.2 cm^2 (BD Biosciences, Heidelberg, Germany). After cultivation for several hours at 37°C, pH-adjusted medium was added and the system was transferred to an incubator (5% CO_2, 95% humidity). After a second incubation, primary human keratinocytes were added on top of the collagen matrix. On the next day, the construct was lifted to the air-liquid interface and medium was changed to a differentiation medium [64]. After 2 days, we induced a wound by scratching the epidermal layer with a needle. The injured constructs were incubated with pH-defined media (pH_e 6.5 and 7.4). To mimic *in vivo* wound healing more closely, 50 µl of the media (simulating wound fluid) were applied onto the epidermal layer. After 48 h, the skin constructs were punched, embedded in tissue freezing medium and kept at -80°C overnight. Subsequently, the skin constructs were cut vertically into slices (10 µm thickness, Frigocut 2800 N, Leica, Bensheim, Germany) and stained with conventional haematoxylin and eosin (H&E).

Microfluidic cell migration assays

Human primary epidermal foreskin keratinocytes were cultivated (37 °C, 5% CO_2) in EpiLife Medium supplied with 1:100 human keratinocyte growth supplement (HKGS, S0015, Life Technologies, Darmstadt, Germany). Cells were passaged every 2-3 days and used for migration experiments at passage 4 or earlier. Microfluidic channels (µ-Slides Chemotaxis 3D, ibidi, Martinsried, Germany) were coated with 70 µg ml^{-1} Fibronectin (Sigma, Germany), dried, and filled with 2-3 x 10^6 cells ml^{-1}. The cells adhered for 2-4 h before the pH_e-gradient was established by filling the two feeding reservoirs of the µ-Slides with Medium 199 (Life Technologies, Darmstadt, Germany) adjusted to pH_e 7.4 and 6.4, which was supplemented with 1:100 HKGS and 5 or 50 µM 2´,7´-bis-(2-carboxyethyl)-5-(and-6)-carboxyfluorescein (BCECF, Life Technologies, Darmstadt, Germany) for pH_e-visualization.

Cell migration and pH_e-gradient stability was monitored at 37 °C and ambient CO_2 conditions for a time period of 14 or 16 h by using a fully automated microscope system (Cell^R, Olympus, Hamburg, Germany) equipped with a 4 x phase-contrast objective (UPLFLN4XPH/0.13, Olympus, Hamburg, Germany). Phase-contrast images were taken every 2 min. Fluorescence images (λ_{ex} 434/17 nm and 492/18 nm, λ_{em} 530/20 nm) were taken alternately at 1 or 30 frames h^{-1} and at 10 or 300 ms exposure time, respectively. Cell migration data analysis was performed using ImageJ software (http://rsbweb.nih.gov/ij/) including the plug-ins Manual Tracking (F. Cordeliers, Institut Curie, Orsay, France) for imaging single-cell migration tracks, and Chemotaxis Tool (ibidi, Martinsried, Germany) to calculate migration velocity, yFMI, accumulated distance, and endpoint y. We used Daniel´s XL toolbox (http://xltoolbox.sourceforge.net) plug-in for Microsoft Excel (Microsoft Corporation, Redmond, WA, USA) to spread scatter plots. The Cell^R image processing software (OlympusSIS, Muenster, Germany) was used for ratiometric analysis of BCECF fluorescence images.

ELISAs

Adult human epidermal keratinocytes (Gibco) were cultured in triplicates under different pH_e. 150 µl supernatants of cell culture were collected after 48 h. Samples were tested using a 16-Plex human cytokine array (Quansys, Logan, UT, USA) according to manufacturer´s protocols. Chemiluminescence images were acquired by BioRad Versa Doc 4000 MP workstation (Bio-Rad, Munich, Germany) using a gain of 2X, binning of 1X1 and auto exposure time settings. Images were exported as 16 bit TIFF raw data for quantitative analysis using the Q-View software (Quansys).

Tissue harvesting

Punch biopsies from wound margins, wound centers, and intact surrounding tissue were taken from patients with chronic venous wounds (ulcers). Wound samples were cut in half along a central line to allow sufficient specimens for immunohistochemistry (IHC), quantitative reverse transcription PCR (qRT-PCR) and Western blots. Allprotect Tissue Reagent (Qiagen, Germantown, MD, USA) was used for preservation.

Histology and Immunofluorescence

Chronic wound biopsies were fixed in paraformaldehyde and routinely processed for paraffin embedding. After blocking with 5% BSA in phosphate buffered saline supplemented with 0.1% Tween 20, sections were incubated with primary antibodies (NHE1 and ATP6V1B1/B2: Santa Cruz Biotechnology; MCT1: Millipore, Billerica, MA, USA) at room temperature for 1 h followed by several washes in PBS and incubation with fluorescently-labelled secondary antibodies, namely Alexa Fluor 594 goat anti-rabbit IgG (H+L) and Alexa Fluor 488 goat anti-mouse

IgG (H+L) (Invitrogen). Images were acquired using an Olympus Bx63 epifluorescence microscope (100x/1.4 NA objective), and image processing (intensity adjustment only, quantitatively equal for all samples) was performed in Adobe Photoshop (Adobe Systems).

RNA and Protein Isolation

Total RNA and proteins were isolated from wound biopsies from human patients using the RNeasy Mini Kit (Qiagen) according to the manufacturer's instructions. RNA aliquots were stored in a -80 °C freezer and extracted protein was stored at -20 °C.

Quantitative Reverse Transcription PCR (qRT-PCR)

For gene expression analysis, isolated total RNA was reverse-transcribed using Sensiscript RT Kit (Qiagen), and cDNA-transcripts were amplified by qPCR using SYBR Green (Applied Biosystems, Cheshire, UK) and primers designed using Primer-BLAST from NCBI. Triplicate samples were used. Expression levels of mRNA were evaluated using the comparative threshold cycle (Ct) method as normalized to β-actin. Relative expression levels of mRNA were calculated between tissue sections.

Western Blots

To assess protein expression, proteins isolated from each patient's wound section were fractionated by 10% sodium dodecyl sulfate-polyacrylamide gel electrophoresis (SDS-PAGE) and transferred to a polyvinylidene difluoride (PVDF) membrane. Blots were then probed with respective primary antibodies specific for each protein: β-actin (A5316 from Sigma–Aldrich; NHE1, MCT-1 and ATP6V1B1/B2 from Santa Cruz Biotechnology, CA, USA). Dilutions were made according to the manufacturer's recommendation. After incubation with respective primary antibodies, the membranes were washed in tris-buffered saline supplemented with 0.1% Tween 20 and incubated with the appropriate secondary antibodies (Sigma-Aldrich) followed by development with the BCIP/NBT phosphatase substrate system (Pierce Biotechnology, Rockford, IL). β-actin served as loading control.

Statistics

We used Sigma Plot 11.0 (Systat Software Inc., Chicago, IL, USA) for all analyses. Data are given as mean ± standard error of the mean (s.e.m.) except otherwise denoted. We considered a p-value below 0.05 as significant. Results were marked as significant with asterisks within the graphs.

We utilized one-way ANOVA and post-hoc Tukey-testing to analyze differences between mean pH_e-values in the 5 defined wound regions. One-way ANOVA and post-hoc Holm-Sidak testing were conducted to assess for statistical differences in proliferation and viability of keratinocytes at varying pH_e. To check for differences in migration velocity, y-FMI, directionality, and endpoint y, we performed one-way ANOVA on ranks and post-hoc Dunn´s testing. Multiplex ELISA results were analyzed using one-way ANOVA and post-hoc Tukey-tests or one-way ANOVA on ranks and Dunn´s post-hoc test. To detect differences in qPCR data, one-way ANOVA and post-hoc Tukey tests were used.

Supplementary Material

Additional File 1:
Figures S1-S10. Tables S1-S2. Still Images for Movies.
http://www.thno.org/v04p0721s1.pdf
Additional File 2:
Movie S1.
http://www.thno.org/v04p0721s2.avi
Additional File 3:
Movie S2.
http://www.thno.org/v04p0721s3.avi
Additional File 4:
Movie S3.
http://www.thno.org/v04p0721s4.avi
Additional File 5:
Macro S1.
http://www.thno.org/v04p0721s5.atn

Acknowledgments

The work was supported by grants of the German Research Foundation (DFG, BA 3410/3-1, BA 3410/4-1, SCHA 1009/7-1, WO 669/9-1), and the ReForM-B program (S.S., University Medical Center Regensburg, Regensburg, Germany). The work was supported by the German Research Foundation DFG within the funding program open access publishing. We thank Beate Morgenstern (Fraunhofer IBMT, Potsdam, Germany) for cell culture assistance and Heiko Siegmund (Center for Electron Microscopy, Institute of Pathology, University Medical Center Regensburg, Regensburg, Germany) for his work on transmission electron microscopic imaging.

Author contributions

S.S., R.J.M., O.S.W., and P.B. designed research. S.S. conceived functional experiments. S.S., R.J.M., M.K., S.C.K., S.G., O.F., S.K., J.R.S., K.W., K.T.W., M.A., U.S., and J.S. performed experiments. S.S., R.J.M., M.K., O.F., J.R.S, S.F.P., and P.B. analyzed the data. C.M., L.P., C.D., M.G., M.B., O.S.W., and M.L. helped to analyze data. S.S., O.S.W. and P.B. obtained grant support. R.J.M., M.K., S.C.K., S.G., O.F., S.K., J.R.S., S.F.P., and P.B. wrote parts of the manuscript.

S.S. compiled and wrote the final manuscript.

Competing Interests

The authors have declared that no competing interest exists.

References

1. Gurtner GC, Werner S, Barrandon Y, Longaker MT. Wound repair and regeneration. Nature. 2008; 453: 314-21.
2. Jacinto A, Martinez-Arias A, Martin P. Mechanisms of epithelial fusion and repair. Nat Cell Biol. 2001; 3: E117-23.
3. Singer AJ, Clark RA. Cutaneous wound healing. N Engl J Med. 1999; 341: 738-46.
4. Martin P. Wound healing - aiming for perfect skin regeneration. Science. 1997; 276: 75-81.
5. Martins VL, Caley M, O'Toole EA. Matrix metalloproteinases and epidermal wound repair. Cell Tissue Res. 2012.
6. Bickers DR, Lim HW, Margolis D, Weinstock MA, Goodman C, Faulkner E, et al. The burden of skin diseases: 2004 a joint project of the American Academy of Dermatology Association and the Society for Investigative Dermatology. J Am Acad Dermatol. 2006; 55: 490-500.
7. Sen CK, Gordillo GM, Roy S, Kirsner R, Lambert L, Hunt TK, et al. Human skin wounds: a major and snowballing threat to public health and the economy. Wound Repair Regen. 2009; 17: 763-71.
8. Behm B, Babilas P, Landthaler M, Schreml S. Cytokines, chemokines and growth factors in wound healing. J Eur Acad Dermatol Venereol. 2012; 26: 812-20.
9. Schreml S, Szeimies RM, Prantl L, Landthaler M, Babilas P. Wound healing in the 21st century. J Am Acad Dermatol. 2010; 63: 866-81.
10. Niethammer P, Grabher C, Look AT, Mitchison TJ. A tissue-scale gradient of hydrogen peroxide mediates rapid wound detection in zebrafish. Nature. 2009; 459: 996-9.
11. Stefonek TJ, Masters KS. Immobilized gradients of epidermal growth factor promote accelerated and directed keratinocyte migration. Wound Repair Regen. 2007; 15: 847-55.
12. Wenczak BA, Lynch JB, Nanney LB. Epidermal growth factor receptor distribution in burn wounds. Implications for growth factor-mediated repair. J Clin Invest. 1992; 90: 2392-401.
13. Hinman CD, Maibach H. Effect of Air Exposure and Occlusion on Experimental Human Skin Wounds. Nature. 1963; 200: 377-8.
14. Winter GD. Formation of the scab and the rate of epithelization of superficial wounds in the skin of the young domestic pig. Nature. 1962; 193: 293-4.
15. Winter GD. Effect of Air Exposure and Occlusion on Experimental Human Skin Wounds. Nature. 1963; 200: 378-9.
16. Winter GD, Scales JT. Effect of air drying and dressings on the surface of a wound. Nature. 1963; 197: 91-2.
17. Muller P, Schier AF. Extracellular movement of signaling molecules. Dev Cell. 2011; 21: 145-58.
18. Schreml S, Szeimies RM, Karrer S, Heinlin J, Landthaler M, Babilas P. The impact of the pH value on skin integrity and cutaneous wound healing. J Eur Acad Dermatol Venereol. 2010; 24: 373-8.
19. Horikoshi T, Balin AK, Carter DM. Effect of oxygen on the growth of human epidermal keratinocytes. J Invest Dermatol. 1986; 86: 424-7.
20. Pentland AP, Marcelo CL. Modulation of proliferation in epidermal keratinocyte cultures by lowered oxygen tension. Exp Cell Res. 1983; 145: 31-43.
21. Xia YP, Zhao Y, Tyrone JW, Chen A, Mustoe TA. Differential activation of migration by hypoxia in keratinocytes isolated from donors of increasing age: implication for chronic wounds in the elderly. J Invest Dermatol. 2001; 116: 50-6.
22. Schreml S, Szeimies RM, Prantl L, Karrer S, Landthaler M, Babilas P. Oxygen in acute and chronic wound healing. Br J Dermatol. 2010; 163: 257-68.
23. Vander Heiden MG, Cantley LC, Thompson CB. Understanding the Warburg effect: the metabolic requirements of cell proliferation. Science. 2009; 324: 1029-33.
24. Walpole GS. An Improved Hydrogen Electrode. Biochem J. 1914; 8: 131-3.
25. Lee D, Khaja S, Velasquez-Castano JC, Dasari M, Sun C, Petros J, et al. In vivo imaging of hydrogen peroxide with chemiluminescent nanoparticles. Nat Mater. 2007; 6: 765-9.
26. Nakai J, Ohkura M, Imoto K. A high signal-to-noise Ca(2+) probe composed of a single green fluorescent protein. Nat Biotechnol. 2001; 19: 137-41.
27. Saito K, Chang YF, Horikawa K, Hatsugai N, Higuchi Y, Hashida M, et al. Luminescent proteins for high-speed single-cell and whole-body imaging. Nat Commun. 2012; 3: 1262.
28. Meier RJ, Schreml S, Wang XD, Landthaler M, Babilas P, Wolfbeis OS. Simultaneous photographing of oxygen and pH in vivo using sensor films. Angew Chem Int Ed Engl. 2011; 50: 10893-6.
29. Schreml S, Meier RJ, Weiss KT, Cattani J, Flittner D, Gehmert S, et al. A sprayable luminescent pH sensor and its use for wound imaging in vivo. Exp Dermatol. 2012; 21: 951-3.
30. Schreml S, Meier RJ, Wolfbeis OS, Landthaler M, Szeimies RM, Babilas P. 2D luminescence imaging of pH in vivo. Proc Natl Acad Sci U S A. 2011; 108: 2432-7.
31. Schreml S, Meier RJ, Wolfbeis OS, Maisch T, Szeimies RM, Landthaler M, et al. 2D luminescence imaging of physiological wound oxygenation. Exp Dermatol. 2011; 20: 550-4.
32. Wang XD, Wolfbeis OS. Optical methods for sensing and imaging of oxygen: materials, spectroscopies and applications. Chem Soc Rev. 2014; [Epub ahead of print].
33. Mateescu A, Wang Y, Dostalek J, Jonas U. Thin hydrogel films for optical biosensor applications. Membranes. 2012; 2: 40-69.
34. Biswas S, Roy S, Banerjee J, Hussain SR, Khanna S, Meenakshisundaram G, et al. Hypoxia inducible microRNA 210 attenuates keratinocyte proliferation and impairs closure in a murine model of ischemic wounds. Proc Natl Acad Sci U S A. 2010; 107: 6976-81.
35. Fitsialos G, Bourget I, Augier S, Ginouves A, Rezzonico R, Odorisio T, et al. HIF1 transcription factor regulates laminin-332 expression and keratinocyte migration. J Cell Sci. 2008; 121: 2992-3001.
36. Straseski JA, Gibson AL, Thomas-Virnig CL, Allen-Hoffmann BL. Oxygen deprivation inhibits basal keratinocyte proliferation in a model of human skin and induces regio-specific changes in the distribution of epidermal adherens junction proteins, aquaporin-3, and glycogen. Wound Repair Regen. 2009; 17: 606-16.
37. Liang CC, Park AY, Guan JL. In vitro scratch assay: a convenient and inexpensive method for analysis of cell migration in vitro. Nat Protoc. 2007; 2: 329-33.
38. Zengel P, Nguyen-Hoang A, Schildhammer C, Zantl R, Kahl V, Horn E. mu-Slide Chemotaxis: a new chamber for long-term chemotaxis studies. BMC Cell Biol. 2011; 12: 21.
39. Gillitzer R, Goebeler M. Chemokines in cutaneous wound healing. J Leukoc Biol. 2001; 69: 513-21.
40. Gallucci RM, Sloan DK, Heck JM, Murray AR, O'Dell SJ. Interleukin 6 indirectly induces keratinocyte migration. J Invest Dermatol. 2004; 122: 764-72.
41. Boedtkjer E, Bunch L, Pedersen SF. Physiology, pharmacology and pathophysiology of the pH regulatory transport proteins NHE1 and NBCn1: similarities, differences, and implications for cancer therapy. Curr Pharm Des. 2012; 18: 1345-71.
42. Pedersen SF, O'Donnell ME, Anderson SE, Cala PM. Physiology and pathophysiology of Na+/H+ exchange and Na+ -K+ -2Cl- cotransport in the heart, brain, and blood. Am J Physiol Regul Integr Comp Physiol. 2006; 291: R1-25.
43. Cardone RA, Casavola V, Reshkin SJ. The role of disturbed pH dynamics and the Na+/H+ exchanger in metastasis. Nat Rev Cancer. 2005; 5: 786-95.
44. Webb BA, Chimenti M, Jacobson MP, Barber DL. Dysregulated pH: a perfect storm for cancer progression. Nat Rev Cancer. 2011; 11: 671-7.
45. Endres RG, Wingreen NS. Accuracy of direct gradient sensing by single cells. Proc Natl Acad Sci U S A. 2008; 105: 15749-54.
46. Firtel RA, Chung CY. The molecular genetics of chemotaxis: sensing and responding to chemoattractant gradients. Bioessays. 2000; 22: 603-15.
47. Franca-Koh J, Devreotes PN. Moving forward: mechanisms of chemoattractant gradient sensing. Physiology (Bethesda). 2004; 19: 300-8.
48. Schneider IC, Haugh JM. Quantitative elucidation of a distinct spatial gradient-sensing mechanism in fibroblasts. J Cell Biol. 2005; 171: 883-92.
49. Schneider IC, Haugh JM. Mechanisms of gradient sensing and chemotaxis: conserved pathways, diverse regulation. Cell Cycle. 2006; 5: 1130-4.
50. Yang Y, Sourjik V. Opposite responses by different chemoreceptors set a tunable preference point in Escherichia coli pH taxis. Mol Microbiol. 2012; 86: 1482-9.
51. Paradise RK, Lauffenburger DA, Van Vliet KJ. Acidic extracellular pH promotes activation of integrin alpha(v)beta(3). PLoS One. 2011; 6: e15746.
52. Paradise RK, Whitfield MJ, Lauffenburger DA, Van Vliet KJ. Directional cell migration in an extracellular pH gradient: a model study with an engineered cell line and primary microvascular endothelial cells. Exp Cell Res. 2013; 319: 487-97.
53. Trompezinski S, Denis A, Vinche A, Schmitt D, Viac J. IL-4 and interferon-gamma differentially modulate vascular endothelial growth factor release from normal human keratinocytes and fibroblasts. Exp Dermatol. 2002; 11: 224-31.
54. Sarangarajan R, Shumaker H, Soleimani M, Le Poole C, Boissy RE. Molecular and functional characterization of sodium--hydrogen exchanger in skin as well as cultured keratinocytes and melanocytes. Biochim Biophys Acta. 2001; 1511: 181-92.
55. Halestrap AP. Monocarboxylic Acid transport. Compr Physiol. 2013; 3: 1611-43.
56. Wu L, Xia YP, Roth SI, Gruskin E, Mustoe TA. Transforming growth factor-beta1 fails to stimulate wound healing and impairs its signal transduction in an aged ischemic ulcer model: importance of oxygen and age. Am J Pathol. 1999; 154: 301-9.
57. Sundaram GM, Common JE, Gopal FE, Srikanta S, Lakshman K, Lunny DP, et al. 'See-saw' expression of microRNA-198 and FSTL1 from a single transcript in wound healing. Nature. 2013; 495: 103-6.
58. Burdick JA, Murphy WL. Moving from static to dynamic complexity in hydrogel design. Nat Commun. 2012; 3: 1269.
59. Neri D, Supuran CT. Interfering with pH regulation in tumours as a therapeutic strategy. Nat Rev Drug Discov. 2011; 10: 767-77.

60. Ludwig MG, Vanek M, Guerini D, Gasser JA, Jones CE, Junker U, et al. Proton-sensing G-protein-coupled receptors. Nature. 2003; 425: 93-8.
61. Tomura H, Mogi C, Sato K, Okajima F. Proton-sensing and lysolipid-sensitive G- protein-coupled receptors: a novel type of multi-functional receptors. Cell Signal. 2005; 17: 1466-76.
62. Arwert EN, Hoste E, Watt FM. Epithelial stem cells, wound healing and cancer. Nat Rev Cancer. 2012; 12: 170-80.
63. Harris KL, Bainbridge NJ, Jordan NR, Sharpe JR. The effect of topical analgesics on ex vivo skin growth and human keratinocyte and fibroblast behavior. Wound Repair Regen. 2009; 17: 340-6.
64. Kuchler S, Henkes D, Eckl KM, Ackermann K, Plendl J, Korting HC, et al. Hallmarks of atopic skin mimicked in vitro by means of a skin disease model based on FLG knock-down. Altern Lab Anim. 2011; 39: 471-80.

SUPPLEMENTARY MATERIAL

for

Luminescent Dual Sensors Reveal Extracellular pH-Gradients and Hypoxia on Chronic Wounds That Disrupt Epidermal Repair

Stephan Schreml, Robert J. Meier, Michael Kirschbaum,
Su Chii Kong, Sebastian Gehmert, Oliver Felthaus,
Sarah Küchler, Justin R. Sharpe, Kerstin Wöltje,
Katharina T. Weiß, Markus Albert, Uwe Seidl, Josef Schröder,
Christian Morsczeck, Lukas Prantl, Claus Duschl,
Stine Falsig Pedersen, Martin Gosau, Mark Berneburg,
Otto S. Wolfbeis, Michael Landthaler, Philipp Babilas

Contents

1. SUPPLEMENTARY FIGURES

Figure S1

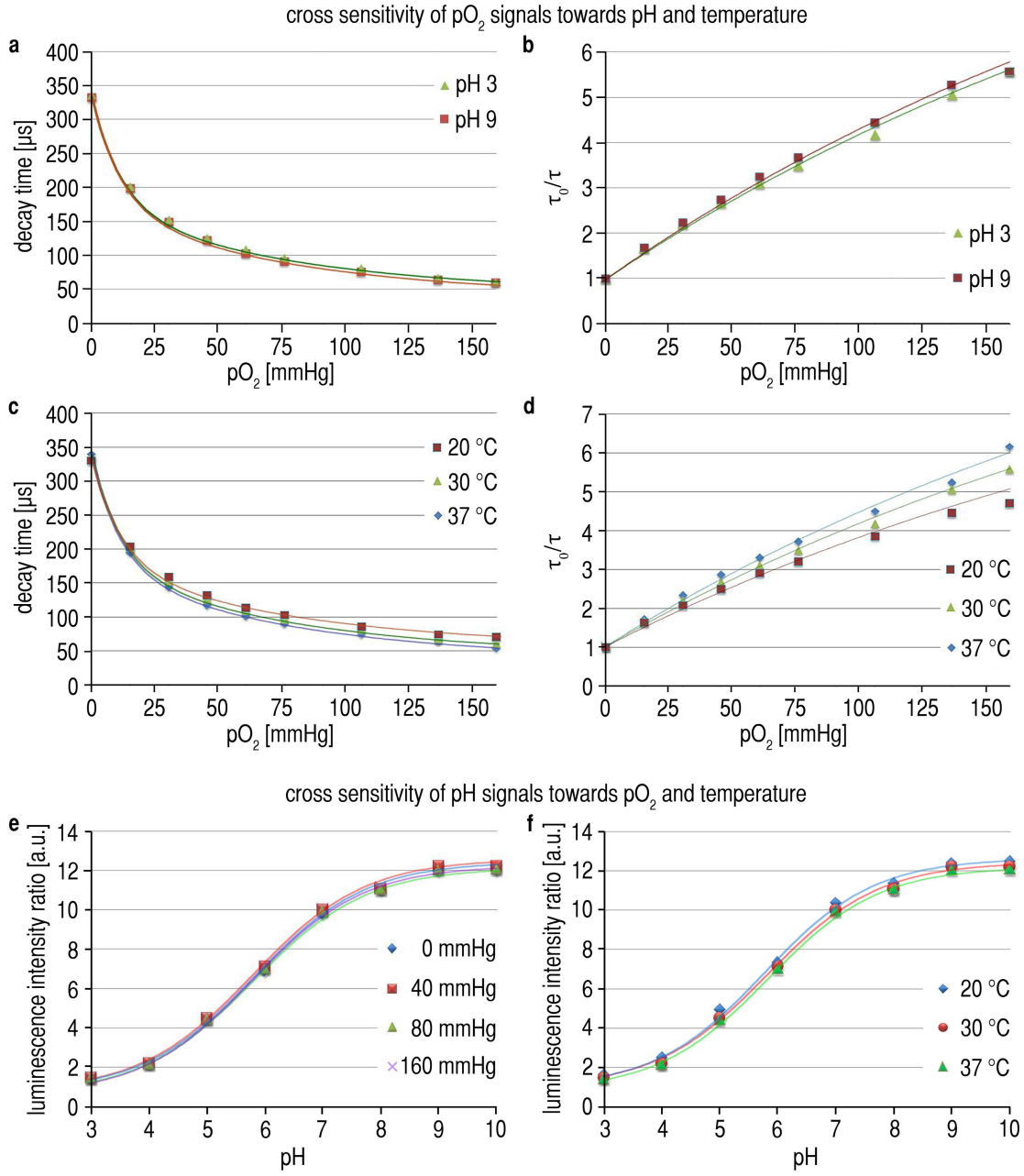

Figure S1: Cross-sensitivity of pO_2/pH-signals and temperature sensitivity. (**A**,**B**) The (**A**) luminescence decay time and the (**B**) Stern-Volmer-Plot of luminescence lifetime ratios τ/τ_0 (τ = luminescence lifetime at respective pO_2, τ_0 = luminescence lifetime at 0 mmHg pO_2) of pO_2-signals under varying pO_2 are not affected by changes in pH (pH 3 vs. pH 9). (**C**,**D**) Temperature, also did not change luminescence decay times or lifetime ratios of pO_2-signals. (**E**,**F**) Luminescence intensity ratios of pH-signals remained unchanged at varying (**E**) pO_2 and (**F**) temperatures.

Figure S2

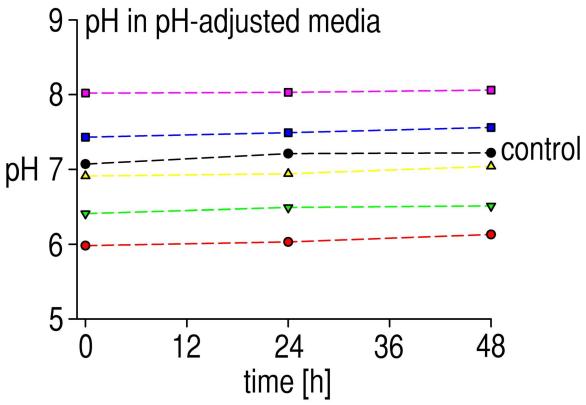

Figure S2: pH-stability of pH-adjusted media. pH was adjusted in culture media to pH 6, 6.5, 7, 7.5, and 8 as outlined in **Materials and Methods**. Stability of pH in pH-adjusted media and of unmodified culture medium was measured with standard pH-electrodes at 0, 24, and 48 h after pH-adjustment. No relevant change of pH in pH-adjusted media was detected over 48 h, the maximum culture time with pH-modified media in all experiments.

Figure S3

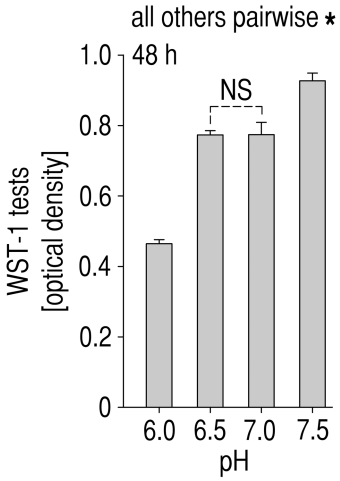

Figure S3: WST-1 tests of keratinocytes cultured in pH-adjusted media. Cell viability increased with rising pH_e, confirming results obtained using ATP-bioluminescence assays (**Fig. 3B**). After 48 h, keratinocyte viability was highest at pH_e of 7.5 and lowest at pH_e of 6.0. n = 6, mean ± s.e.m., NS = not significant, ANOVA $p<0.001$ and $^*p<0.05$ in post-hoc Holm-Sidak tests.

Figure S4

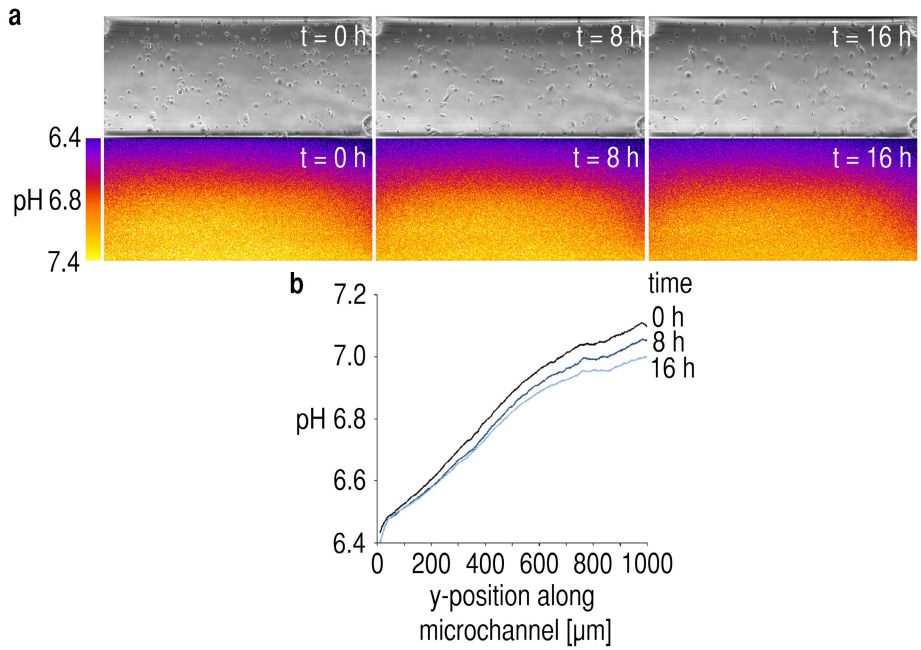

Figure S4: Stability of pH_e-gradients in microfluidic channels. (**A**) Brightfield and pH-visualization (pseudocolor images) of a representative microfluidic keratinocyte migration assay at different time points throughout the experiment. pH_e-gradients were visualized by ratiometric analysis of BCECF pH-indicator fluorescence in the channel fluid. (**B**) Mean pH_e-value along the y axis of the microchannel. pH_e-gradients showed a relatively linear shape and were stable throughout the 16 h time course of the experiment.

Figure S5

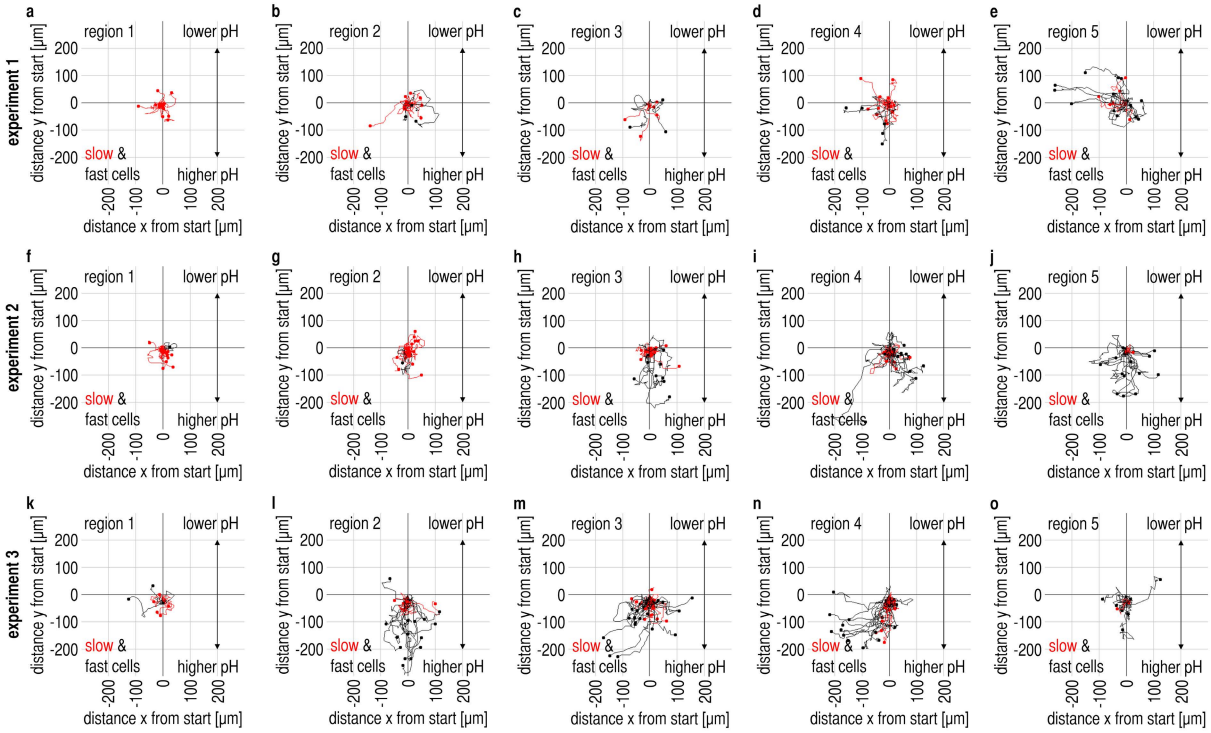

Figure S5: Cell trajectory lines of all performed keratinocyte migration assays. Data of 3 independent experiments (**A**-**E**, **F**-**J**, **K**-**O**) clustered by channel region with increasing mean pH_e from region 1 to region 5 (also see **Movies S1-S3**). Keratinocyte migration was analyzed by time-lapse brightfield microscopy for 16 h. Trajectory lines of the cells were then superimposed (start at x/y = 0 µm) with red lines showing slow migrating cells (mean velocity ≤ 12.6 µm h^{-1}) and black lines showing fast migrating cells (mean velocity > 12.6 µm h^{-1}). Throughout the experiments, the proportion of fast cells increased with rising pH_e. Furthermore, migration distance was markedly higher at high pH_e-values when compared to low pH_e-values as found at the wound periphery.

Figure S6

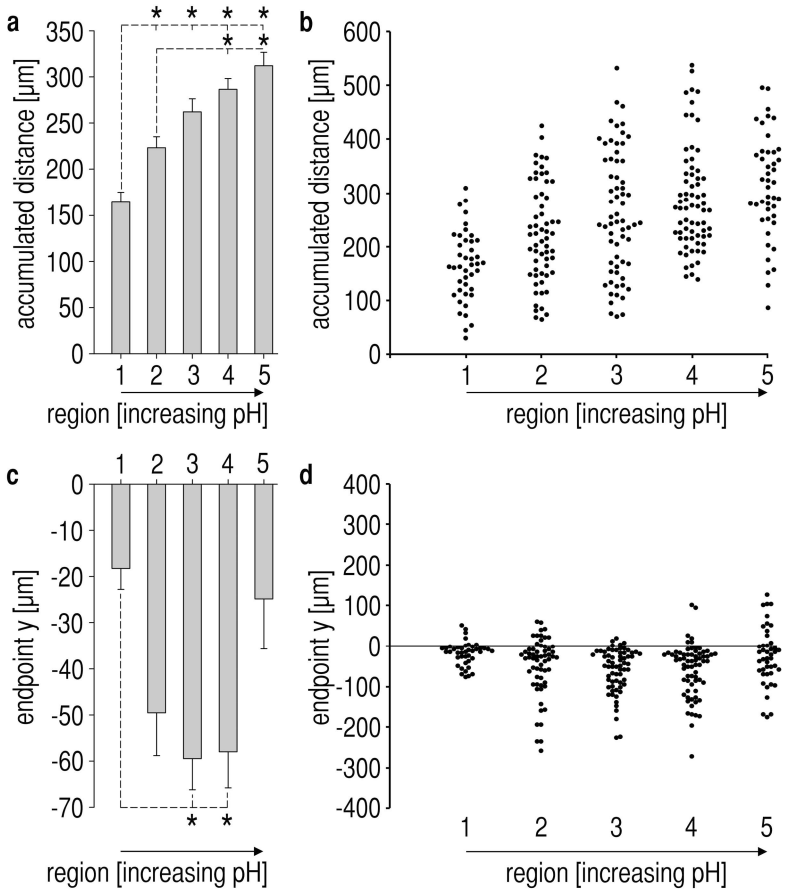

Figure S6: Accumulated distance and endpoint y results of microfluidic migration assays. (**A**,**B**) Mean accumulated distance and respective scatter plot of analyzed single cells (also see **Movies S1-S3**). Accumulated distance increased with higher pH_e and was significantly different between the cells of different channel regions. Mean accumulated distance for cells of region 5 (pH_e ~7.2) was almost two times higher than for cells of region 1 (pH_e ~6.4). (**C**,**D**) Endpoint analysis of y-coordinates of cell positions (along the pH_e-gradient) and respective scatter plot of analyzed single cells. The mean endpoint y decreased from pH_e ~6.4 to ~6.8 (i.e. from region 1 to region 3), and then rose again until pH_e ~7.2 (region 5). Thus, keratinocytes at intermediate pH of ~6.8 exhibit strongest chemotactic activity towards higher pH_e-values when compared with cells at both higher and lower pH_e. The reason for the reduced chemotactic activity towards higher pH_e-values for cells in low pH_e (~6.4) as well as high pH_e (~7.2) might be due to a reduced motility or a reduced driving force for directed migration of these cells, respectively. Number of cells tracked in 3 experiments: region 1 (n = 42), 2 (n = 60), 3 (n = 65), 4 (n = 69), 5 (n = 44). One-way ANOVA on ranks $p<0.001$, *$p<0.05$ in post-hoc Dunn´s test.

Figure S7

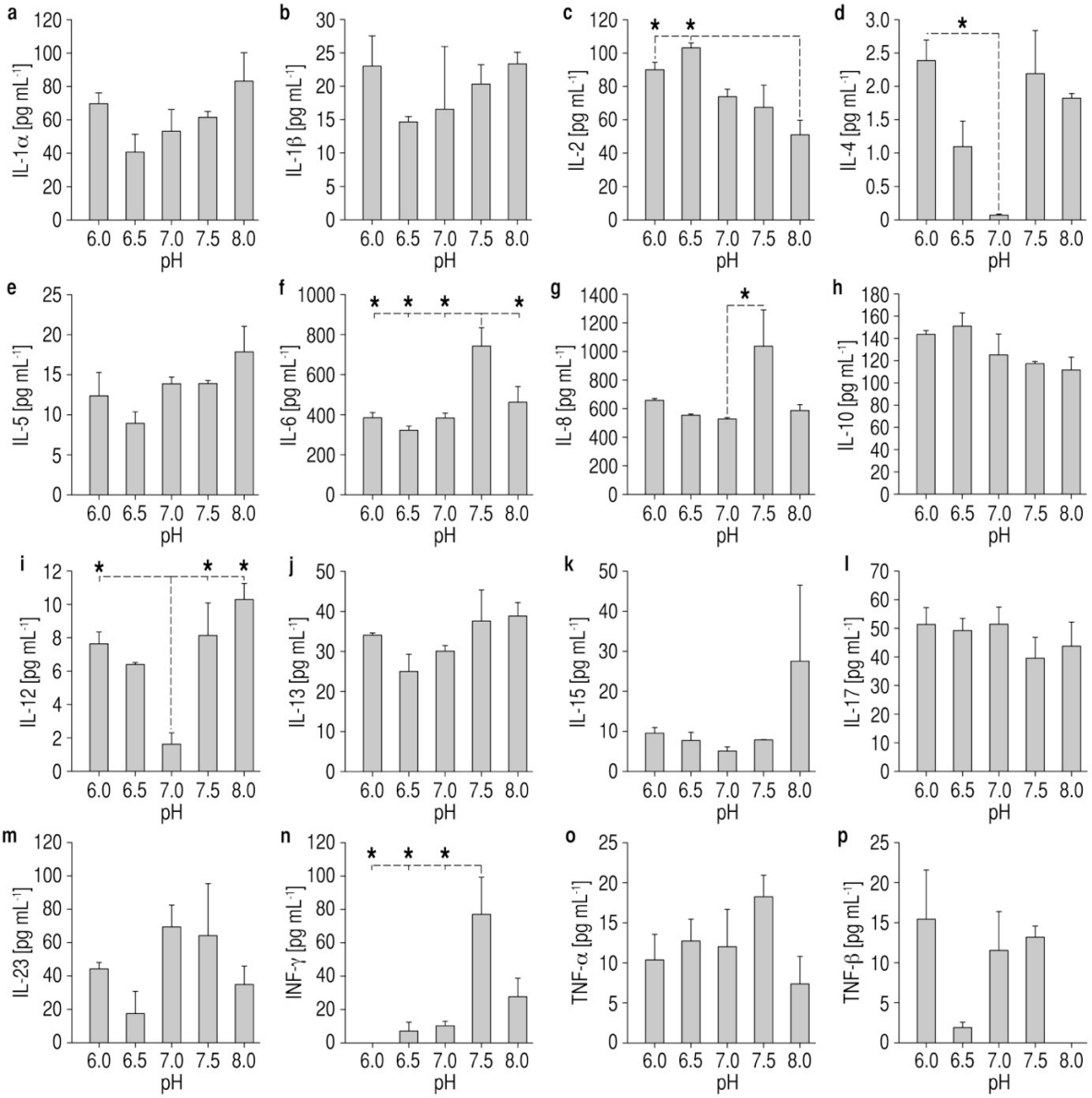

Figure S7: Cytokine and chemokine secretion patterns of keratinocytes under varying pH_e. We found that (**D**,**I**) IL-4 and IL-12 were markedly downregulated at pH_e 7.0 when compared to lower or higher pH_e-values. Additionally, keratinocytes cultured at the predominantly high pH_e of 7.5, as found at the wound centers, secreted markedly more (**F**,**G**) IL-6 and IL-8 (important direct and indirect mediators of keratinocyte proliferation/migration) when compared with those at lower pH_e (as found at the wound periphery). Another interesting finding was that (**N**) interferon-γ (INFγ) release from keratinocytes increased with rising pH_e. INFγ is known to stimulate VEGF production of keratinocytes, and VEGF is a key molecule in neoangiogenesis during healing. At low pH_e, as found at the wound periphery, we found low levels of INFγ in keratinocyte supernatants.

Figure S8

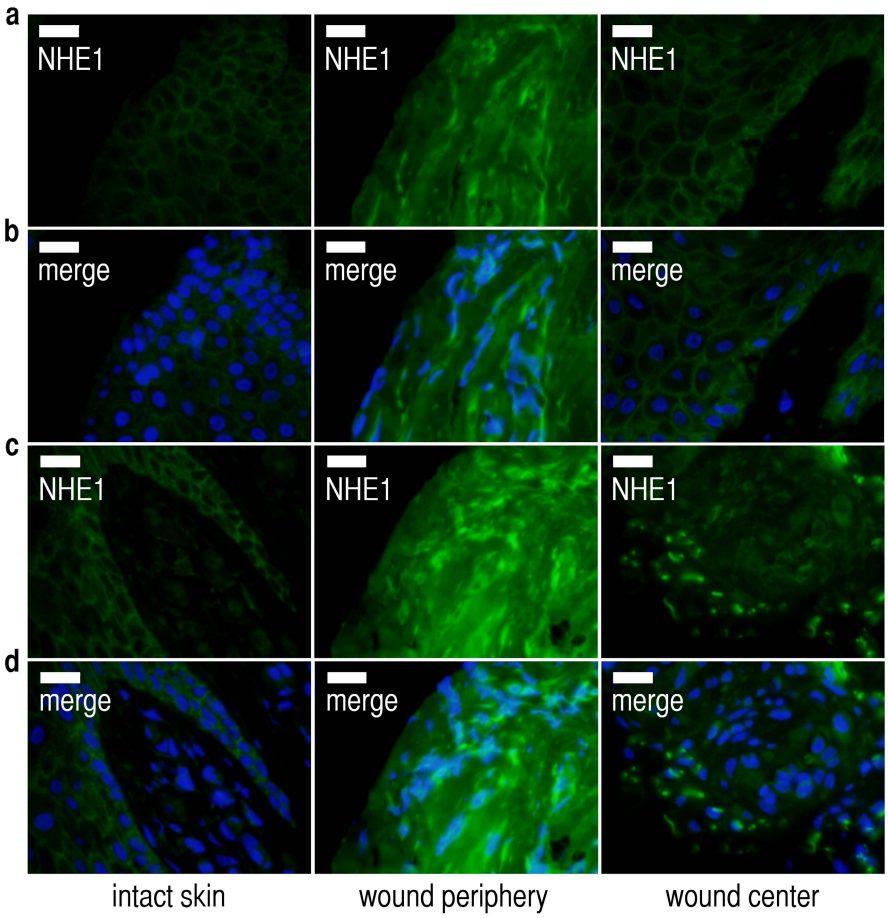

Figure S8: Expression and localization of pH_e-regulatory NHE1 in chronic wounds. (**A**-**D**) Additional immunofluorescence images of intact skin, peripheral wound tissue, and central wound tissue from chronic wound patients. Sections were counterstained with (**B**,**D**) DAPI (blue) for nuclei staining. Scale bars, 20 µm. (**A**,**C**) NHE1 is strongly upregulated in peripheral wound tissue as compared to intact skin and tissue from the wound center.

Figure S9

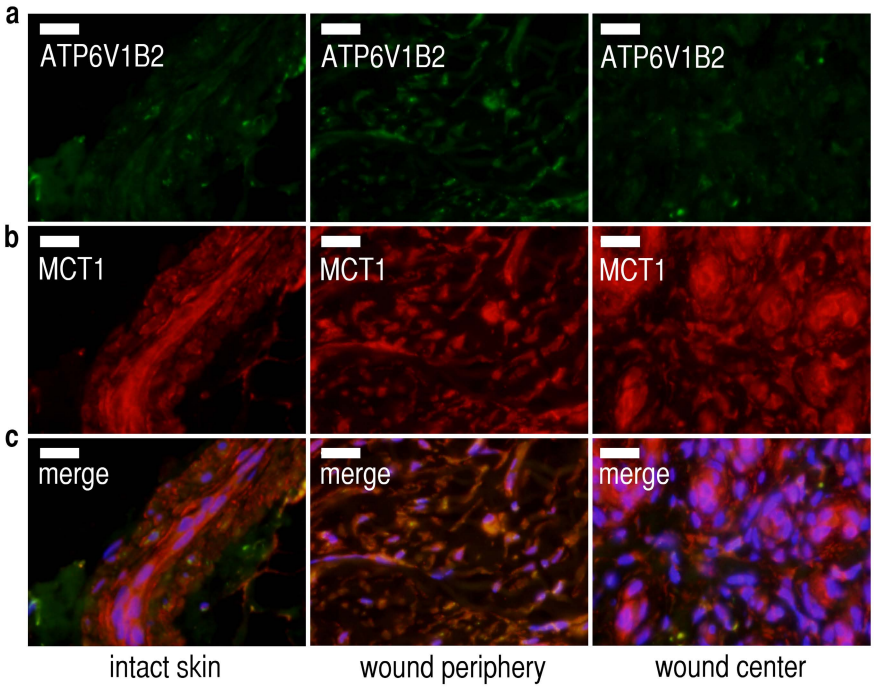

Figure S9: Expression of proton transporters ATP6V1B2 and MCT1 in intact skin and chronic wounds.

(**A**-**C**) Additional immunofluorescence images of intact skin, peripheral wound tissue, and central wound tissue from chronic wound patients. Sections were counterstained with (**C**) DAPI (blue) for nuclei staining. Scale bars, 20 µm. n = 3. There were virtually no differences in the expression of the (**A**) plasma membrane vacuolar-type ATPases subunit b2 (ATP6V1B2, green) and (**B**) the (H^+-lactate) monocarboxylate transporter 1 (MCT1, red) between intact skin and wound sections.

Figure S10

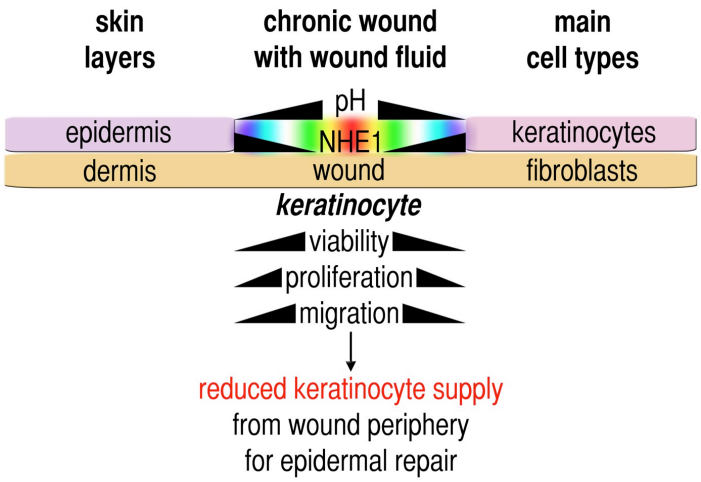

Figure S10: NHE1-generated pH_e-gradients in chronic wounds and their impact on epidermal barrier repair. We found that pH_e rises with increasing distance from the wound margins. These pH_e-gradients are predominantly generated via centrifugally rising NHE1-expression, a proton transpoter crucial for extracellular acidification. The pH_e-gradients found reduce cell viability, proliferation and migration velocity of keratinocytes at the wound periphery. Centripetal keratinocyte recruitment from the wound periphery is critically reduced by the observed pH_e-gradients in chronic wounds, thus disrupting epidermal barrier repair.

2. SUPPLEMENTARY TABLES

Table S1: Characteristics of patients with chronic venous wounds for imaging

No. Sex Age (yrs)	Time of wound persistence (months until imaging)	Localization Size (greatest diameter within wound)	Bacterial colonization (last documented swab, alphabetically)	Main causative disease	Concomitant diseases (as documented in patient history, alphabetically)
1 f 67	14	left medial lower leg 3 cm	enterobacter cloacae pseudomonas aeruginosa staphylococcus aureus	chronic venous insufficiency (CVI)	adipositas permagna arterial hypertension diabetes mellitus type II tinea pedis type IV allergies - amerchol - benzalkonium chloride - cetylstearyl alcohol - formaldehyde - lanolin alcohols
2 m 79	> 60	right lateral lower leg 6 cm	pseudomonas aeruginosa staphylococcus aureus	chronic venous insufficiency (CVI)	arterial hypertension chronic osteomyelitis hypercholesterinemia microangiopathy
3 f 79	48	left medial lower leg 7 cm	not available (12/11 measurement, 08/11 pseudomonas aeruginuosa)	chronic venous insufficiency (CVI)	hypothyreoidism tinea pedis type IV allergies - amerchol - benzocaine - budesonide - fragrance mix - gentamicin sulfate - nickel - peru balm - phenyl mercury borate xerosis cutis
4 f 73	64	left medial lower leg 4 cm	staphylococcus aureus	chronic venous insufficiency (CVI)	adipositas arterial hypertension hyperkalemia onychomycosis
5 f 73	41	right ventral lower leg 8 cm	corynebacterium spp. proteus mirabilis pseudomonas aeruginosa staphylococcus aureus	chronic venous insufficiency (CVI)	adipositas permagna diabetes mellitus type II diabetic nephropathy erysipelas (of the lower right leg) tinea pedis hypothyreoidism
6 f 63	24	right lateral lower leg 7.5 cm	pseudomonas aeruginosa serratia marcescens	chronic venous insufficiency (CVI)	arterial hypertension hypercholesteremia hyperuricemia
7 f 77	14	left lateral lower leg 5 cm	staphylococcus aureus	chronic venous insufficiency (CVI)	adipositas permagna arterial hypertension chronic heart failure chronich renal failure combined aortic vitium diabetes mellitus type II diabetic micorangiopathy diabetic nephropathy diabetic polyneuropathy mitral valve insufficieny postthrombotic syndrome

8 m 53	150	left medial lower leg 6 cm	enterobacter cloacae staphylococcus aureus	chronic venous insufficiency (CVI)	diabetes mellitus type II local fasciectomy postthrombotic syndrome resection of saphenous magna vein smoking thrombophlebitis
9 m 51	13	right medial lower leg 4 cm	staphylococcus aureus	chronic venous insufficiency (CVI)	deep leg vein thrombosis (15 years ago)
10 f 66	33	right medial lower leg 3 cm	pseudomonas aeruginosa serratia marcescens	chronic venous insufficiency (CVI)	arterial hypertension chronic heart failure hypercholesteremia onychomycosis percutaneous transluminal coronary angioplasty thyroid subfunction tinea pedis type IV allergies - amerchol - benzoyl peroxide - cetylpyridiniumchloride - cetylstearyl alcohol - cobalt - fragrance mix - framycetin - kanamycin - lanolin alcohols - mercury - neomycin - nickel - nystatin - peru balm - propylene glycole - sodium disulfite - tolu balm - tree moss - turpentine xerosis cutis

Table S2: Characteristics of patients with chronic venous wounds for biopsies

No. Sex Age (yrs)	**Time of wound persistence (months until biopsy)**	**Localization Size (greatest diameter within wound)**	**Bacterial colonization (last documented swab, alphabetically)**	**Main causative disease**	**Concomitant diseases (as documented in patient history, alphabetically)**
1 m 65	36	right medial malleolus 5 cm	coagulase-negative staphylococci staphylococcus aureus	chronic venous insufficiency (CVI)	COPD diabetes mellitus type II type IV allergies - amerchol - butyl paraben - benzoyl peroxide - cetylstearyl alcohol - cocamidopropyl betain - diazolidinyl urea - 1,3-diphenylguanidin - dodecyl gallate - ethyl paraben - imidazolidinyl urea - lanolin alcohol - methyl paraben - panthenol - polidocanol - paraben - propylene glycol - propyl paraben - sodium metabisulfite - t-butyl hydrochinone - triethanolamine
2 m 67	27	left medial malleolus 7 cm	proteus mirabilis pseudomonas aeruginosa streptococcus agalactiae	chronic venous insufficiency (CVI)	diabetes mellitus type II diabetic polyneuropathy
3 f 78	60	left medial lower leg 3 cm	pseudomonas aeruginosa staphylococcus aureus	chronic venous insufficiency (CVI)	adipositas arterial hypertension diabetes mellitus type II onychomycosis type IV allergies - amerchol - benzalkonium chloride - cetylstearyl alcohol - fragrance mix - lanolin alcohol - thiuram

3. SUPPLEMENTARY STILL IMAGES FOR MOVIES

Still Image for Movie S1

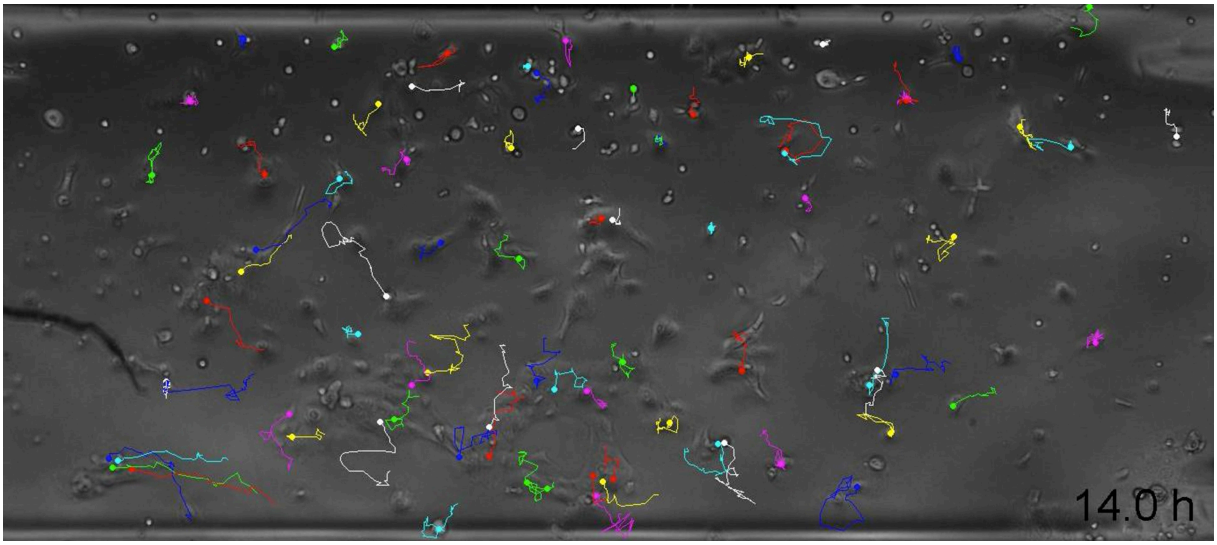

Still Image for Movie S1: Time-lapse microscopy image sequences of microfluidic keratinocyte migration assay 1. Human epidermal keratinocytes were seeded into a fibronectin-coated microfluidic channel and were analyzed for cell migration under no-flow condition while a pH_e-gradient was established in y-direction from pH ~6.4 (upper channel boundary) to pH ~7.2 (lower channel boundary). Trajectories of the analyzed cells are superimposed on the original images. Frame rate, ~2.5 frames h^{-1}. Throughout all experiments (experiments 1-3 in **Movies S1-S3**), migration velocity rose from low to high pH_e. Accumulated migration distances were highest at high pH_e of ~7.2 when compared to pH_e of ~6.4. A detailed analysis of the results is shown in **Fig. 3E-L** and **Figs. S5** and **S6**.

Still Image for Movie S2

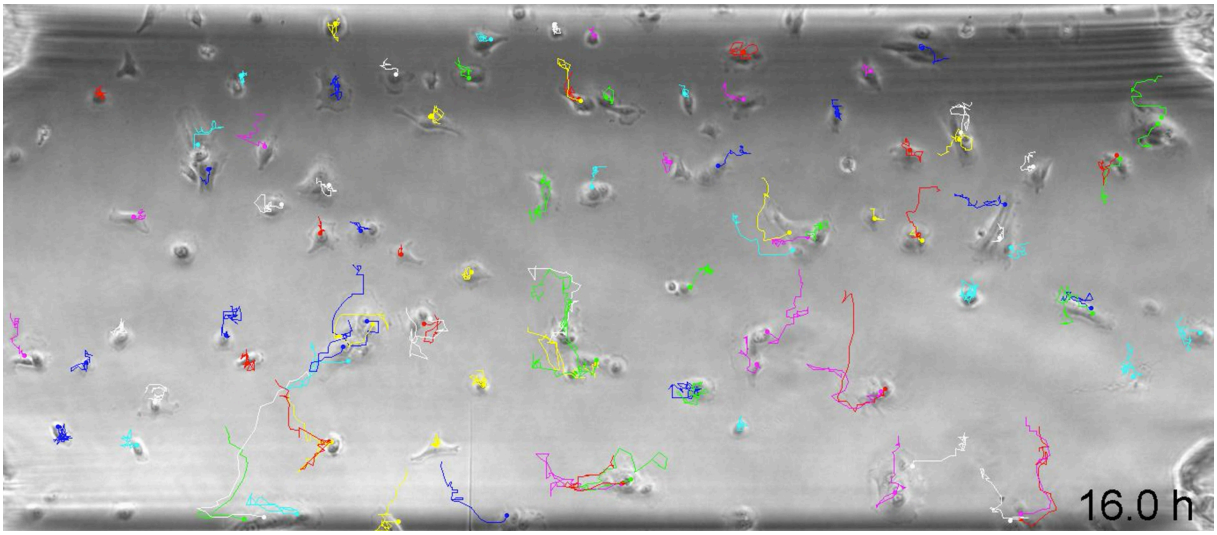

Still Image for Movie S2: Time-lapse microscopy image sequences of microfluidic keratinocyte migration assay 2. Human epidermal keratinocytes were seeded into a fibronectin-coated microfluidic channel and were analyzed for cell migration under no-flow condition while a pH_e-gradient was established in y-direction from pH ~6.4 (upper channel boundary) to pH ~7.2 (lower channel boundary). Trajectories of the analyzed cells are superimposed on the original images. Frame rate, ~2.5 frames h^{-1}. Throughout all experiments (experiments 1-3 in **Movies S1-S3**), migration velocity rose from low to high pH_e. Accumulated migration distances were highest at high pH_e of ~7.2 when compared to pH_e of ~6.4. A detailed analysis of the results is shown in **Fig. 3E-L** and **Figs. S5** and **S6**.

Still Image for Movie S3

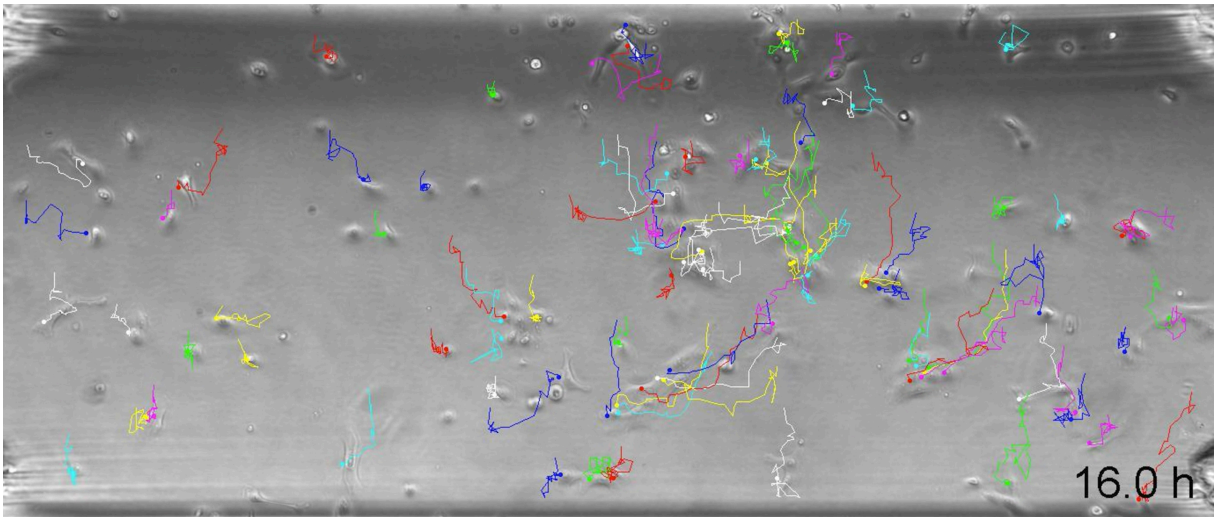

Still Image for Movie S3: Time-lapse microscopy image sequences of microfluidic keratinocyte migration assay 3. Human epidermal keratinocytes were seeded into a fibronectin-coated microfluidic channel and were analyzed for cell migration under no-flow condition while a pH_e-gradient was established in y-direction from pH ~6.4 (upper channel boundary) to pH ~7.2 (lower channel boundary). Trajectories of the analyzed cells are superimposed on the original images. Frame rate, ~2.5 frames h^{-1}. Throughout all experiments (experiments 1-3 in **Movies S1-S3**), migration velocity rose from low to high pH_e. Accumulated migration distances were highest at high pH_e of ~7.2 when compared to pH_e of ~6.4. A detailed analysis of the results is shown in **Fig. 3E-L** and **Figs. S5** and **S6**.

4. SUPPLEMENTARY MACRO LEGEND

Macro S1: Macro for 2D pO_2/pH_e-calculation. The self-programmed Photoshop macro contains three sub-macros ("macro for preparation", "macro for slicing", and "macro for measurement") that have to be executed following the protocol described in **Materials and Methods**. The first action adapts and standardizes the size of each image and transfers the previously defined wound margins to the raw data TIFF-images. The second action divides raw data from the entire wound into five consecutive regions, starting from the wound periphery towards the center. The final action measures the grayscale mean values of the slices and the entire wound surface and records these values in a CSV-table that can be further used in Excel to convert and calculate respective pO_2/pH_e-data.